Saint Petersburg State University Hamburg University

Russian-German Master Program for Polar and Marine Sciences
POMOR

Master thesis

Reconstruction of Late Quaternary paleo-current activity on southern Lomonosov Ridge (Arctic Ocean) and its paleoenvironmental significance

Elena Popova

Saint Petersburg / Hamburg, 2019

Scientific supervisors

Dr. Alexey Krylov, Saint Petersburg State University

Prof. Dr. Rüdiger Stein, Alfred Wegener Institute Helmholtz Center for Polar and Marine Research

Table of contents

Reconstruction of Late Quaternary paleo-current activity on southern Lomonosov Ridge (Arctic Ocean) and its paleoenvironmental significance

Elena Popova
Master Program for Polar and Marine Sciences POMOR / 050406 Ecology and environmental management

Supervisors:
Dr. Alexey Krylov, Saint Petersburg State University
Prof. Dr. Rüdiger Stein, Alfred Wegener Institute Helmholtz Center for Polar and Marine Research

As polar areas play an important role in the global climate and related water mass circulation patterns, it is very useful to closely study recent and past changes in Arctic Ocean circulation characteristics. Despite this importance, the number of studies on paleo-currents is still scarce, mainly due to the remoteness of this area. The present study reconstructs the strength of paleo-currents activity in a channel on the Southern Lomonosov Ridge near Siberian shelf of the Arctic Ocean and connects these data with the paleoenvironmental history.

The material was gained during Polarstern Expedition 115/2 in September-October 2018 (Stein, 2019). Three gravity cores about 4 to 6 m length were used together with surface sediments from box-corers in order to acquire a continuous record for the profile of the channel system. Echo-sounding Parasound data were studied as well to complement the data obtained from the sedimentary records.

The "sortable silt (10-63 μm) mean grain-size approach" was applied as a main proxy for paleo-current activity. The basic principle of this approach is that ocean currents cannot transport sand fraction (63 μm - 2 mm), while particles finer than 10 μm form aggregates, and their primary size is not present. Thus, these fractions are excluded in this approach (cf., McCave et al., 1995). In order to get accurate results of the grain-size distribution of the silt fraction, grain-size was measured using a SediGraph III Plus. Mean sortable silt values are correlated with percentages of sortable silt and the amount of the sand fraction in order to determine core segments with the highest current sorting and the influence of IRD input, respectively. In addition, total organic carbon (TOC) content was measured as a parameter for organic matter burial/preservation.

All three cores were mainly composed of fine (clayey silt and silty clay) sediments, although numerous coarser layers were revealed. TOC contents was quite low (about 0.2% in

average), typically for the Arctic Ocean. Based on the preliminary age model (Stein, 2019), changes in current activities can be reconstructed from the end of MIS 7 to present time. Sortable silt mean size experienced significant fluctuations during the whole period indicating events with higher current strength, and decreases in energy, proving that the channel has been a pathway for water mass transport from the Amundsen Basin into the Makarov Basin. The current speed proxy, together with echo-sounding and bathymetry data as well as the age model, allowed to reconstruct changes in strength of the flow in three levels at the bottom of the channel. Thus, both lateral and vertical migration of the position of the current was revealed. During MIS 7 and MIS 6, the current was probably strong but relatively high above the bottom, leading to a uniform deposition. After that, it started to deepen and move to the south-west, narrowing down the moat and enhancing deposition at the flank during the following stages (MIS 5 to 2?). During MIS 1, the "wide-flow" mode established again, covering the site with sediments equally.

Periodical fluctuations of the current's strength were discovered: slightly higher speeds were more typical during interglacials and terminations followed by decreases during cold (glacial) periods. This succession is considered to be related to the Atlantic Water inflows, which in turn depended on the climatic conditions. During interglacials Atlantic Intermediate Water was probably formed closer to the north; due to an enhanced stratification caused by ice melting it could reach further east and may have crossed the Lomonosov Ridge. During cold stages, on the other hand, the situation was the opposite, and the migration was inhibited.

The attempt to determine the IRD in the record showed a few IRD peaks during the end of MIS 4 and MIS 5. Yet, the precise division of a coarse fraction into current-sorted and ice-rafted was not performed.

Реконструкция позднечетвертичных палеотечений в южной части хребта Ломоносова (Северный Ледовитый океан) и их влияние на палеосреду

Попова Елена Александровна
Магистерская программа «Полярные и морские исследования» («ПОМОР») / 050406 «Экология и природопользование»
Выпускная квалификационная работа магистра

Научные руководители:
Крылов Алексей Алексеевич, доцент СПбГУ, кафедра осадочной геологии
Рюдигер Штайн (Prof. Dr. Rüdiger Stein), профессор, Институт им. Альфреда Вегенера, Центр полярных и морских исследований в Объединении им. Гельмгольца, Германия

Поскольку полярные области имеют большое значение для климата планеты и связанной с ним системы океанических течений, важно изучать изменения характеристик циркуляции в Северном Ледовитом океане как в настоящее время, так и в прошлом. Несмотря на это, изучение палеотечений здесь ведётся не так активно, в основном, из-за удалённости региона. В данной работе проведена реконструкция активности палеотечений в эрозионном канале в южной части хребта Ломоносова около сибирского участка континентального шельфа Северного Ледовитого океана; полученная информация использовалась для расшифровки эволюции условий осадконакопления. Материал был собран во время экспедиции PS115/2 (сентябрь – октябрь 2018) научно-исследовательского ледокола «Поларштерн» (Stein, 2019). Три колонки донных осадков длиной 4–6 м были отобраны при помощи гравитационной трубки, для отбора поверхностных проб в тех же локациях использовался бокс-корер. Помимо проб осадков, был использован сейсмоакустический профиль, полученный с помощью системы Parasound.

В качестве главного «прокси» для активности палеотечений использовался показатель «средний размер сортируемого алеврита (10-63 мкм)». Основной принцип заключается в том, что океанические течения, как считается, не могут переносить песчаную фракцию (63 мкм - 2 мм) на дальние расстояния, в то время как частицы мельче 10 мкм образуют агрегаты, и их первичный размер сложно измерить. Таким образом, данные фракции исключаются при анализе (McCave et al., 1995). Для получения наиболее точных результатов по гранулометрическому составу алевритовой фракции, размер частиц был измерен при помощи SediGraph III Plus. Была проведена корреляция значений среднего размера сортируемого алеврита с

процентным содержанием этой фракции и песка для определения участков колонок с максимальной сортировкой осадков под воздействием течения и проверки наличия частиц ледникового разноса соответственно. Также было измерено содержание общего органического углерода (TOC) в качестве параметра для оценки степени захоронения/сохранности органического вещества.

Колонки сложены в основном тонкими осадками (глинистый алеврит и алевритовая глина), хотя слои грубозернистых осадков также были замечены. Содержание органического углерода достаточно низкое (в среднем около 0,2%), что типично для арктических осадков. Использование «прокси» палеотечений вместе с данными сейсмоакустики, батиметрии и стратиграфии (предварительная возрастная модель описана в Stein, 2019) позволило реконструировать изменения интенсивности потоков водных масс в канале с конца морской изотопной стадии (МИС) 7 до настоящего времени. В частности, было обнаружено горизонтальное и вертикальное перемещение позиции течения. Во время МИС 7 и 6 течение, вероятно, было сильным, но протекало высоко относительно дна, что приводило к равномерному осадконакоплению. Затем произошло понижение уровня течения и его движение на юго-запад, что привело к сужению канала там и усилению осадконакопления на склоне. Во время МИС 1 снова установился режим широко распределённого течения, приведя к образованию равномерного слоя осадков на дне. Были обнаружены периодические колебания интенсивности течения: более сильные скорости оказались характерными для межледниковий и дегляциаций, тогда как для ледниковых периодов было типично их снижение. Такой порядок связывается с режимом притока Атлантических вод, который в свою очередь зависит от климатических условий. Во время межледниковий Атлантические Промежуточные воды вероятно формировались ближе к северу; кроме того, благодаря усиленной стратификации, вызванной таянием льда, они могли проникать дальше на восток и пересекать хребет Ломоносова по каналу. Ситуация была противоположной в ледниковые периоды, и течение вод ослаблялось.

Попытка выявить частицы ледового разноса показала несколько пиков в МИС 4 и 5. Тем не менее, точное разделение грубой фракции на сортированные течением частицы и ледовый разнос не было выполнено и является предметом последующих исследований.

1. Introduction

Global climate change is a complex phenomenon which involves all components of environment as they are all interconnected. Such aspects of climate change as fluctuations of air and water temperature, composition of atmosphere, onset of glaciers and deglaciations have been studied actively since the methods were invented (Coope et al., 1999; Lewis et al., 2007; Mora et al. 2007; Spielhagen et al., 2004; Thomas et al., 2018). Changes in water circulation is another feature inevitably accompanying climate cycles because warming of the atmosphere causes the glaciers to melt increasing inflow of cold freshwater and changing the balance in the whole circulation system. The scale of changes depends on geography, geomorphology, ice volume, water composition (Knutz, 2008; Jakobsson et al., 2014; Jennings et al., 2006) Polar areas are known to be important components of the global water circulation pattern as all centers of deep-water formation were discovered to be placed in high latitudes (e.g., Smillie et al., 2018). The present circulation of deep water as well as surface currents in the Arctic Ocean have been studied by many authors (Aagaard et al., 1985; Laukert et al., 2017; Rudels, 2018; Spall, 2013; Woodgate, 2012). Changes of the circulation patterns in the Arctic Ocean in the geological past in connection with glaciations and deglaciations, on the other hand, have been covered scarcely so far, supposedly because of the remoteness of the area and technical difficulties of coring and drilling. There are a few studies that reconstruct circulation regime changes here on both a million- and thousand-years scale (Andrews, 2011; Hoffmann et al., 2019; Jakobsson et al., 2007; Lantzsch et al., 2017). All studies related to current activity dynamics, which use the approach applied in the presented research, cover areas south of 72° N, in the Arctic Ocean particularly – only shelf slopes zones (McCave and Andrews, 2019); an example of such reconstruction on the southern Lomonosov Ridge (81° N) in a deep part of the ocean is presented here.

Apart from being cold and isolated, the Arctic Ocean is distinguished by its in general low sedimentation rate of 1 cm/ka due to low primary productivity (Stein and Macdonald, 2004), what makes the study of the past conditions via reconstructions more complicated. Being a distinctive oceanographic feature with high energy, intermediate and deep-water currents (or contour currents) leave a clear trace in sediments, a combination of erosion and accumulation processes in one place called a contourite (Smillie et al., 2018; Rebesco et al., 2014; Stow et al., 2008) As there is a gradient of energy across the slope, sediments are inevitably accumulating along the direction of the flow resulting in a complex of layers of increased sedimentation rate (Bianchi and McCave, 1999). Therefore, having a better resolution, deep

current sediments are a reliable source of information for paleoreconstructions, especially in the Arctic (Knutz, 2008).

The Lomonosov Ridge, being the largest geomorphological feature in the Arctic Ocean, divides it into the Eurasian and Amerasian basins. The size of the ridge makes it a significant barrier for water flows. That is why any channel is considered to be a pathway for deep or intermediate water. The aim of this work is to prove the influence of currents on the studied site - a channel in southern Lomonosov Ridge towards the Siberian continental margin - and to reconstruct changes in paleocurrent activity as well as to determine its possible significance to the paleoenvironment. The main approach is using the common for currents reconstruction proxy "sortable silt mean ($\overline{SS}$)" (McCave et al., 1995; McCave and Hall, 2006) to determine periods with a higher or lower speed of water flow. Additionally, total organic carbon (TOC) content was used as a parameter indirectly reflecting production and climate change in the ocean sediments (Clark et al., 1980; Henrich et al., 1989). Physical properties such as wet bulk density and volume-specific magnetic susceptibility were used to create an age model by means of correlation of these characteristics with the core with determined strata age.

2. Study area

2.1. Geography and morphology of the Arctic Ocean

The Arctic Ocean can be defined as an enclosed ocean, and its boundaries are the Eurasian continent, Bering Strait, North America/Canada, Greenland, Fram Strait, and Svalbard, and the shelf break from Svalbard southward to Norway (Fig. 1). More than half of the total area of the ocean (52.7%) is comprised of the shallow continental shelves (Jakobsson et al., 2003). The shelves form shallow, broad (up to 500 km wide) shelf seas, separated by island groups into the Barents Sea, Kara Sea, Laptev Sea, East Siberian Sea, and the Chukchi Sea north of Eurasia. The mean depths of shelf seas are around 50 m or less, except for the roughly 200 m-deep Barents Sea (Mauritzen et al., 2013). The large shelf areas result in a quite small water volume and a shallow mean depth of the entire Arctic Ocean of 1,361 m (Stein, 2008). The Arctic Ocean abyssal plains in turn make up approximately 11.8% of the Arctic Ocean area (Jakobsson, 2002).

The Lomonosov Ridge, with a mean sill depth of 1870 m, separates the Eurasian Basin from the Amerasian Basin (Fig. 1). The Eurasian Basin is divided by the Gakkel Ridge into the Nansen Basin (maximum depth 4000 m) and the Amundsen Basin (maximum depth 4500 m). The Amerasian Basin consists of the Makarov Basin and the large Canada Basin, both reaching down to 4000 m deep, and separated by the Alpha-Mendeleyev Ridge. (Mauritzen et al. 2013; Rudels, 2015)

2.2. Arctic Ocean circulation

Circulation in the Arctic Ocean is conditioned by a few factors such as restricted connection with the World Ocean and distinctive water mass properties. It has been noted that salinity

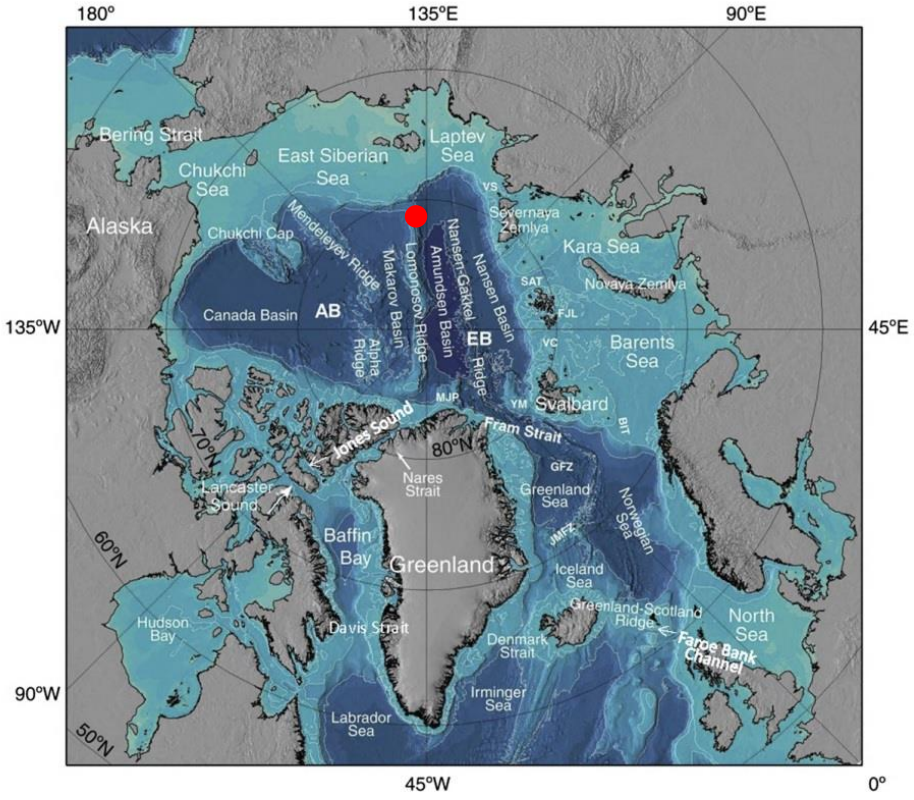

Figure 1. Map of the geographical and bathymetrical features of the Arctic Ocean. AB: Amerasian Basin; BIT: Bear Island Trough (Barents Sea opening); BC: Barrow Canyon; CC: Central Channel; EB: Eurasian Basin; FJL: Franz Josef Land; GFZ: Greenland Fracture Zone; HC: Herald Canyon; MJP: Morris Jessup Plateau, JMFZ: Jan Mayen Fracture Zone; SAT: St. Anna Trough; YP: Yermak Plateau; VC: Victoria Channel; VorC: Voronin Canyon; VS: Vilkitskij Strait; WI: Wrangel Island (Rudels et al., 2015). Red dot marks location of the cores used in the study.

and not temperature dominates in water mass stratification in the Arctic Ocean due to very low temperatures here (Mauritzen et al., 2013; Spall, 2013; Woodgate, 2012), what leads to an evident halocline and makes freshwater input significant. Such conditions led to quite a stable stratification consisting of five layers in general. The upper one is surface or Polar Mixed Layer underlain by halocline in which strong salinity maximum is observed,

sometimes containing Pacific Waters; below Arctic Atlantic Water follows with temperatures above 0°C. Then upper Polar Deep Water is placed representing intermediate water under which various deep waters circulate in different basins (Rudels et al. 1994; Mauritzen et al. 2013).

There are two major gateways connecting the Arctic Ocean with the Atlantic Ocean and the Pacific Ocean: Fram Strait and Bering Strait, respectively (Fig. 2). Fram Strait is 500 km wide and 2600-m deep (Mauritzen et al. 2013) and is the main source of oceanic water in the Arctic Ocean and the only pathway for deep water (Swift and Koltermann, 1988).

Surface water circulation has been studied well most probably due to the presence of the ice (Mauritzen et al., 2013; Jones, 2001; Proshutinsky et al., 2015; Rudels, 2018; Woodgate, 2012). Circulation in the Arctic Ocean is usually described as a cycle of Atlantic Water entering the ocean through Fram Strait and subsequent changes happening to water flow on the way as morphology and other sources of water interfere. For the surface water circulation wind is the major factor. Low-pressure systems above the Eurasian Basin cause a cyclonic movement, supported by freshwater input from the large rivers Ob, Yenisei, Lena, leading to increased ice formation (Mauritzen et al., 2013) that is enriched in the Siberian branch of the Transpolar Drift. The opposite situation is observed over the Amerasian Basin, where the pressure is predominantly high and circulation is anti-cyclonic. Ekman transport – to the right from the wind direction – plays an important role here creating convergence and the Beaufort Gyre. Surface water and ice then leave the gyre into the Transpolar Drift and move to the south through Fram Strait (Rudels, 2018).

Intermediate and deep-water circulation expectedly has a higher connection to the topography. North Atlantic Water flows through the Norwegian Sea where it splits into two parts, one moving to the north of Svalbard, the other – to the south, and merge, reaching the northern part of the Barents Sea in the St. Anna Trough. This water mass moves to the east along the continent as a boundary current circumflexing the Siberian islands. Meeting Lomonosov and Nansen–Gakkel Ridges a branch separates and flows back toward Fram Strait (Rudels et al., 1994; Spall, 2013). The rest continues the flow.

As the Arctic Ocean is divided by the relatively shallow Lomonosov Ridge into the Amerasian and Eurasian basins, and the water circulation is cyclonical and restricted, there is a difference between the water masses of the Amerasian and Eurasian basins (Ikeda et al., 2018). The amount of Pacific Water entering through Bering Strait is not large, nevertheless, it creates a major difference due to its low salinity and density (Rudels, 2018; Woodgate et

al., 2001). At the same time, the isolation is not ultimate. There are estimates that about 5 Sv crosses the Lomonosov Ridge into the Canadian Basin as a boundary current (Rudels et al., 1994; Woodgate, 2012; Woodgate et al., 2001). Moreover, water from the Eurasian Basin enters the Amerasian Basin not only along the slope in a boundary current but at topographical irregularities of the Lomonosov Ridge (Bluhm et al., 2015; Jones, 2001).

The boundary current moving westward reaches the Alpha Ridge and enters the Amerasian Basin where it meets and merges with the cyclonically circulating water in the Makarov Basin. The stream splits into two parts: one following the Lomonosov Ridge and creating a gyre in the Makarov Basin and the other crossing the Lomonosov Ridge and the Amundsen Basin moving toward Greenland (Rudels, 2018; Mauritzen et al. 2013). The water leaves the Arctic Ocean as East Greenland Current in the western Fram Strait, where a major part of Atlantic Water along with some Pacific Water is returned (Rudels, 2018).

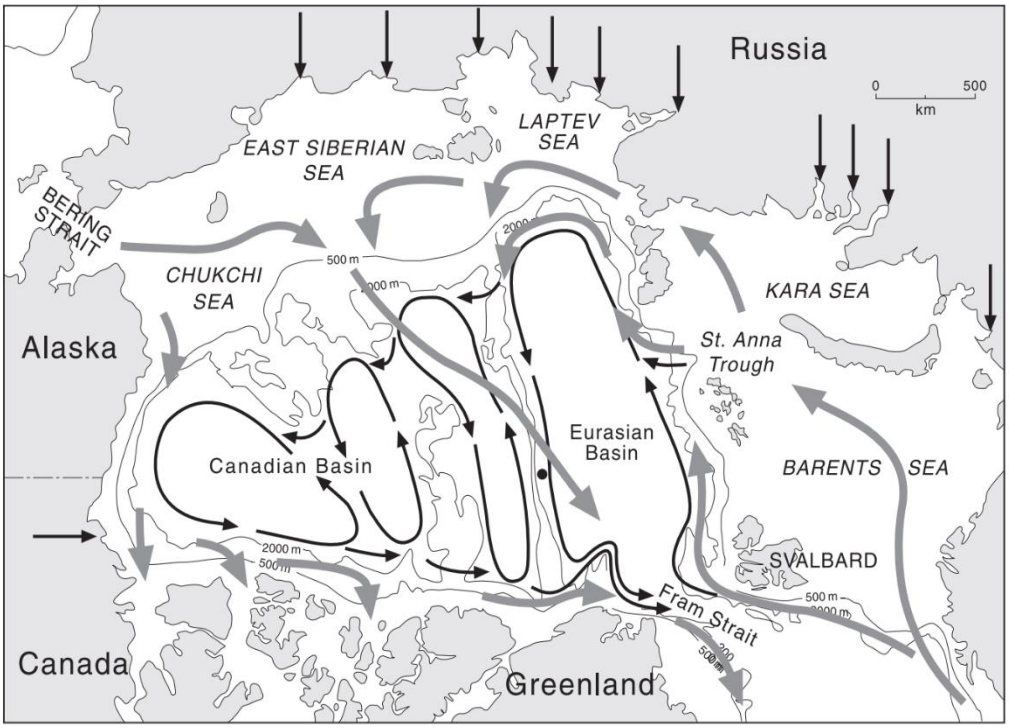

Figure 2. Schematic circulation of surface water (grey arrows) and the Atlantic Layer plus Upper Polar Deep Water to depths of about 1700 m (black arrows). The straight arrows represent the mouths of major rivers (Jones, 2001).

2.2. The Lomonosov Ridge morphology

The Lomonosov Ridge is approximately 1700 km long and 50–200 km wide. Water depth varies significantly from about 1000 m at the ridge crest to 3900–4300 at its base. The shallowest part of the ridge (400 m) is located near Ellesmere-Greenland shelf junction, where 2400 m-deep saddle separates it from the shelf (Piskarev et al., 2018).

The present master thesis work concentrates on the southern part of the Lomonosov Ridge towards the Siberian continental margin, where it divides the Amundsen and Makarov basins. Here the flank of the ridge consists of a series of basement highs stepping down to the basin, considered to be rotated fault blocks active during the continental rifting stage of the formation of the Eurasian Basin. The region is characterized by a complex pattern of ridges and basins. The largest ridge extends south of 84°40’ E. To the south, this ridge splits into two ridges and then dies away rapidly (Cochran et al., 2006).

A narrow channel is located here between 81° to 81° 30’ N and 138° to 142° E in N-W – S-E direction at approximately 1600 - 1700 m water depth (Fig. 1). The studied sediment cores were located across this channel representing three different kinds of sedimentary environments characteristic for a current-influenced deposit: the lower flank with high sedimentation rate (Core 11), the bottom part where the channel is supposed to be erosive with minimum sedimentation rate (Core 13) and a mid-point phase on the slope in between (Core 12) (Fig. 3).

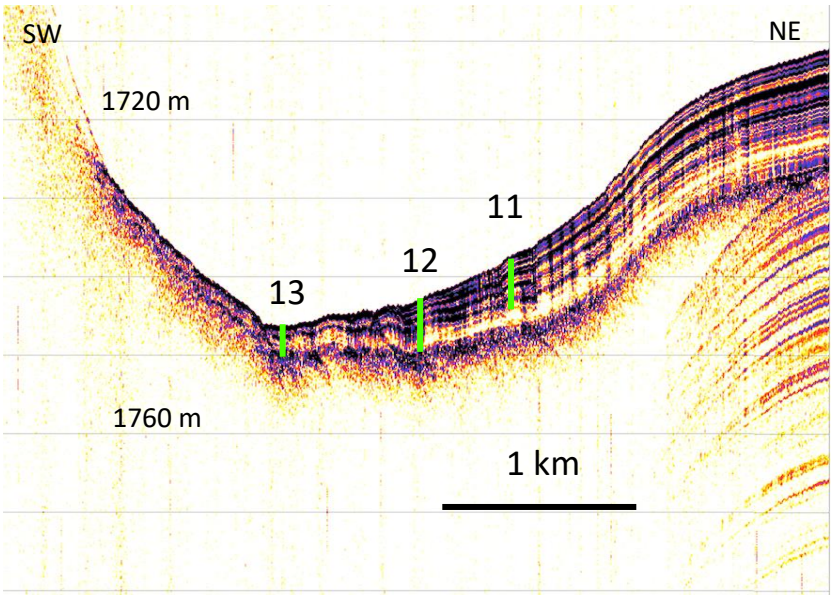

Figure 3. PARASOUND profile across the channel (obtained during Expedition PS 87 in 2014; Stein, 2015), and locations of cores 11, 12 and 13 (recovered during Expedition PS 115/2 in 2018; Stein, 2019). The coring locations were selected based on the PARASOUND survey.

3. Material and methods

3.1. Material

Major part of the material used in the thesis comprises three sediment cores taken by gravity corer (GC or "Schwerelot" – SL) during Polarstern Expedition PS115/2 in September-October 2018 (Stein, 2019): PS 115/2_11-3, PS 115/2_12-1 and PS 115/2_13-2 (the cores will be further referred to as 11, 12, and 13 respectively). The length of the core barrel was 10 m at stations 11 and 12 and 5 m at station 13. As the top of gravity cores is usually considerably disturbed or destroyed, (near-)surface samples were taken by a giant box corer ("Großkastengreifer" – GKG). All three cores were located on a north-eastern slope of a NW-SE oriented channel on the southern Lomonosov Ridge (Fig. 3) (Table 1).

In addition to material taken in 2018, particular data from gravity Core 109 taken during the Polarstern Expedition PS 87 in 2014 (Stein, 2015) were also used. This core was recovered from a flat area with a normal undisturbed pelagic sedimentation to the north of the channel.

Table 1. Gear, recovery, location, water depth and the number of samples of the cores used in the study (Stein, 2019)

Station No	Gear No	Gear	Recovery, cm	Latitude N	Longitude E	Depth (m)	Samples for the study
PS115/2_11	PS115/2_11-1	GKG	48	81,0878	140,9138	1698	1 (surface)
	PS115/2_11-3	SL	624	81,0879	140,9133	1696	64
PS115/2_12	PS115/2_12-2	GKG	36	81,0854	140,8925	1700	1 (surface)
	PS115/2_12-1	SL	643	81,0852	140,8905	1701	43
PS115/2_13	PS115/2_13-1	GKG	39	81,0819	140,8657	1705	1 (surface)
	PS115/2_13-2	SL-5	401	81,0822	140,8639	1706	46

3.2. Cores routine onboard

All the work on material acquisition and analysis is shortly presented in a flow chart (Fig. 4).

Surface samples (0-1cm) were taken from the box corer surface inside an area covered by a plastic tube of 12 cm in diameter and stored in a 100 ml plastic beaker.

Before opening, gravity cores were first run through the Multi-Sensor Core Logger (MSCL), and fractional porosity, p-wave velocity, wet bulk density, and volume-specific magnetic

susceptibility were measured. The latter two parameters were used in this study to correlate the cores with Core 109 in order to create a preliminary age model (Stein, 2019).

After MSCL runs, the cores were cut into work and archive halves. High-quality photographs were taken of both halves. Archive parts were visually described in order to document lithological and structural features as well as color changes (Munsell Soil Colour Chart was used) (Stein, 2019).

Prior to sampling the work halves, locations of samples were chosen thoroughly based on changes in color and lithology along the cores and marked with wooden tooth sticks. Samples were taken by a 10 ml syringe and then put into a plastic beaker. Both surface and core samples were stored at 4°C.

3.3. Laboratory work

Laboratory analysis was performed at the Alfred-Wegener-Institute Helmholtz Centre for Polar and Marine Research in Bremerhaven, Germany, during February-April 2019.

Before the analyses, all samples were freeze-dried at -30°C; 1 g (5 g for surface samples) out of the whole sample was weighed and ground for the TOC analysis.

3.3.1. Total organic carbon (TOC) analysis

Sub-samples of approximately 90 mg were put in ceramic crucibles (in order to prevent contact with carbon) and treated with a few drops of ethanol to increase the wettability, and 500 µl of 37% hydrochloric acid (HCl) to remove the inorganic carbon (carbonate). After that, the samples were heated on a heating plate to 250°C for at least two hours. In order to enhance combustion, iron and wolfram chips were added to every sample.

Eventually, TOC was measured on *Eltra CS 2000 Carbon Sulfur Determinator* calibrated with ALPHA standard 142 (AR4020) (TC = 0.88 – 0.92%). The samples along with the standard 142 (which was placed after each row of 11 samples for an accuracy control) were loaded into a furnace automatically and burned with a stream of pure oxygen at about 1300°C so that CO_2 would emerge. The method is based on the reaction of pure carbon to the emitted gas (Eltra Elemental Analyzers, 2013).

3.3.2. Grain-size analysis

Considering that the main goal of the thesis is determining current activity in the past and the main proxy for that currently is the sortable silt mean ($\overline{SS}$) (cf., McCave and Andrews, 2019), the grain size analysis of fine fraction was to be performed with much attention and

precision. That is why the SediGraph III Plus which measures mass percent of particles in size range 0.523 - 62.5 μm was used, although, such type of grain size analysis requires sediments to be in a condition of a highly saturated suspension (Stein, 1985). Therefore, several steps of preparation were needed to make the samples fit this condition.

The samples were prepared by adding demineralized water and shaking for at least half an hour in order to dissimilate aggregates that could have formed during freeze-drying. After that, the sediments were wet-sieved through a sieve with a mesh size 63 μm in order to divide the sand fraction from silt and clay. The sand fraction was dried at 50°C and weighed so that mass percent of sand could be calculated.

Fine fraction was collected in 5 l plastic bowls. After sedimentation the visibly clear water was removed, and the samples were transferred into 400 ml glass beakers. In order to reduce the amount of water in a suspension, beakers were put into an oven at 50°C. Having reached the possible minimum amount of water in a sample without drying, they were put into 100 ml plastic beakers. They were in turn subject to evaporation again as their smaller volume allowed for sediments to settle down so that visible water separation would happen.

This suspension with a quite high sediment concentration was analyzed using the mentioned above SediGraph III Plus (SediGraph III PLUS Particle Size Analyzer). It calculates the mass percent of particles using Stokes's law on particles settling. The principle of work is as follows: dispersed sediment goes through a transparent plastic cell subject to X-ray beam; the beam's attenuation is measured as a function of time and height, what allows to calculate the distribution of particles (Stein, 1985). Measurement of the grain size during the settling of particles is related to transport and deposition in an environment, making use of the SediGraph suitable for the paleo-current intensity studies (McCave and Hall, 2006).

3.4. Data processing

Excel (MS Office) was used for primary data preparation and evaluation via plotting, and minor calculations. Basic statistical parameters and tables of correlation were calculated in Statistica (StatSoft) software. Graphs were created in Grapher 9. The free software environment for statistical computing and graphics R (https://www.r-project.org) allowed performing interpolation in order to divide fine fraction into subfractions at precise size boundaries (for example, 2 μm between very fine silt and clay) as well as cluster analysis. Such parameters as sortable silt percentage and sortable silt mean size were also calculated in R. Maps and other graphics were created using Inkscape.

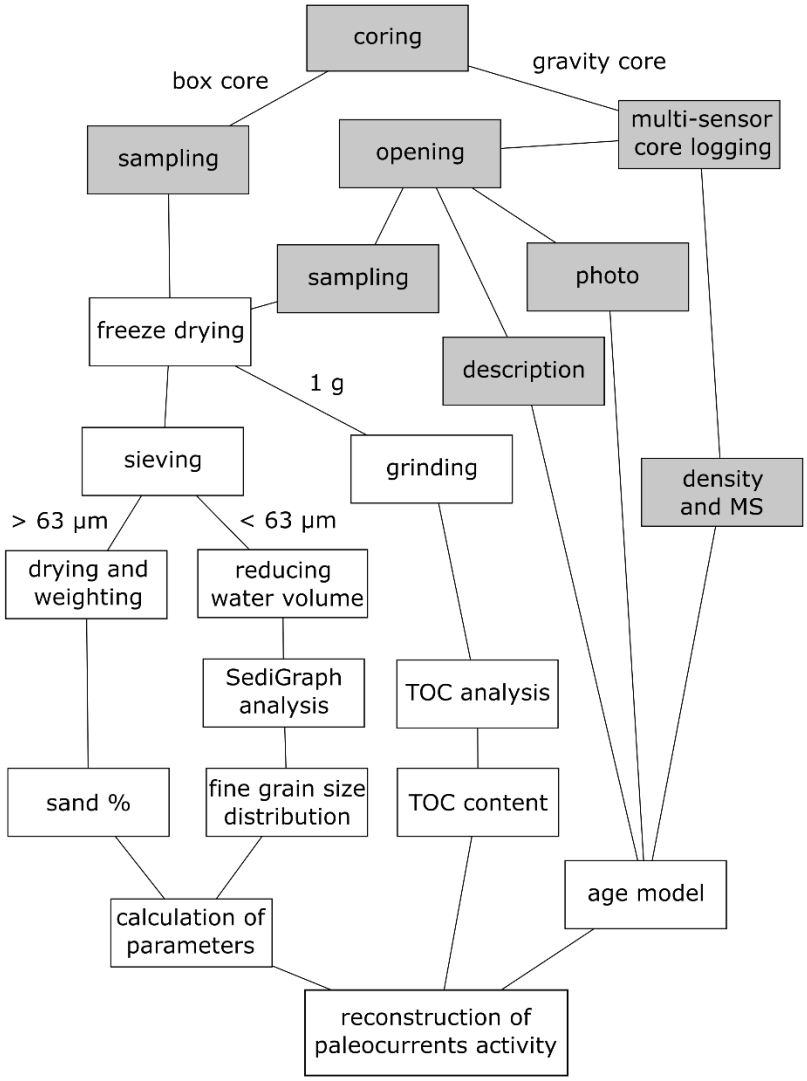

Figure 4. Flow chart of data processing and analysis procedure; blocks with gray fill indicate work onboard the research vessel (Stein, 2019).

3.5. Sortable silt mean size as a proxy: background and calculation

The attempts to quantitatively describe the capability of water flow to transport particles depending on their size have been studied for a long time (Hjulström, 1935; Ledbetter, 1986). Firstly, only the sand fraction had been studied, then, as techniques were becoming more advanced, the analysis of smaller particles became possible. Particles of all size range are to some extent sorted by the water flow as the capacity of the flow to carry material is limited. Large particles settle down quite early in the current flow while fine are carried by the current for long distances. Size of 63 µm has been traditionally used as a boundary between sand and mud, and sand is considered to be too large and heavy to be transported by currents long-distance; thus, particles larger than 63 µm are excluded from the current-transportable fraction despite that very strong currents can transport them (Lamy et al., 2015; Mao et al.,

2018). It has been noted that silt particles less than 10 μm in diameter behave like clay: they are cohesive and form aggregates easily (McCave et al., 1995). In order to detect flow speed, only primary size should be considered, that is why the finest fraction is excluded. Due to these conditions, the size window 10-63 μm is called "sortable silt". It needs to be mentioned that particle size does not reflect the flow direction, only strength, therefore, the term speed is used rather than velocity which is a vector value (McCave, 2008).

The sediments prior to grain-size analysis for this kind of proxy are in most studies treated with at least H_2O_2 to remove organic carbon (McCave et al., 1995) and quite often with HCl and NaOH to delete carbonates and biogenic opal respectively (Lantzsch et al., 2017). In this study though this was not performed because the content of organic material proved to be rather low (see Chapter 4.2).

Sortable silt mean size has been widely used in paleocurrent reconstructions (Hoffmann et al., 2019; Homas et al., 2006; Jonkers at al., 2015; Lamy et al., 2015; Li et al., 2019). Nevertheless, the precise description of its calculation was rarely found in the literature (e.g., McCave and Andrews, 2019). Considering it to be a major parameter in the present research, there is a need to place here a calculation method.

Data on grain size acquired with a SediGraph is represented as a table in which cumulative mass percentages match each measured size. First, data on all particles smaller than 10 μm should be eliminated. Then 50% quantile is found by calculating the mean between maximum and minimum percentage. Finally, the size corresponding to this percentage is found by means of interpolation.

Along with the mean size in a range 10-63 μm, the mean percentage of sortable silt is calculated (SS%). It is the sum of percentages between 10 and 63 μm, which is divided by the total fine fraction (% <63 mm) (McCave and Andrews, 2019). Representation of data in SediGraph allows to calculate it quite easily.

4. Results

4.1. Lithology

In general, all three studied cores are composed of silty clay colored in various shades of brown, olive and gray with thin layers of sand at different intervals basing on visual description (Stein, 2019). Although, the grain size was determined precisely later during the analysis, and it proved that clayey silt is met in the cores at least as often as silty clay, so by silty clay in the description both silty clay and clayey silt are meant. Nevertheless, the feature

of sharp grain size change from fine to coarse particles along the cores is delivered by the description.

Core 11

Fine gray sediments layer of 40 cm thick is observed along with olive silty clay with several sand layers from the bottom to 517 cm. It is followed by light and dark olive gray silty clay, mottled at 517-472 cm. A clear boundary at 439 cm indicates 20 cm thick dark gray layer covered by a 10 cm thick fading gray silty clay. From 429 cm alternating layers of light grayish brown to very dark grayish brown silty clay are observed up to 323 cm, having coarser composition and laminated character of altered silt and sand in the lower part and bioturbation traces at 338-323 cm. Above there is an 80-90 cm layer of yellowish and light olive brown silty clay with few thin sandy layers followed by a pattern of intervening relatively thin brown or very dark gray silty clay layers at 258-255, 130-121.5 and 35-24 cm. Signs of bioturbation are seen at 250-147 cm. The upper 48 cm of 624 cm of Core 11 is represented by very dark and dark brown partly laminated silty clay.

Core 12

Core 12 has similar lithological pattern although with some differences. Layers of grayish-brown and olive gray silty clay are observed from the bottom of 643 cm to 557 cm, laminated in the lower part. Several prominent sand layers are seen between 631 and 590 cm. Above the sediments turn into massive dark gray silty clay, changed by olive gray, light olive brown and yellowish-brown silty clay with bioturbation marks at 426 cm. At 353-331 cm mottled grayish brown silty clay is seen, covered by 10 cm of massive olive gray silty clay and then laminated layers of olive gray and yellowish-brown silty clay. From 280 to 207 cm layers of thin laminated dark grayish-brown silt and sand are seen, followed by a fill of brown silty clay. Very dark grayish-brown and brown layers of silt and sand are observed up to 191 cm, where they are replaced with brown silty clay. At 152 cm a layer of very dark grayish brown and brown silty clay starts with signs of bioturbation yet slightly laminated. Massive light olive brown and brown silt dominates at 137-74 cm, covered by thin layers of sand fining upwards to a three cm thick layer of laminated yellowish-brown silty clay and silt. Then, similarly to Core 11 case, a layer of bioturbated very dark grayish-brown and brown silty clay is met up to 64 cm, after what non-laminated olive brown and brown silty clay is observed. Six cm of laminated olive brown silty clay follow, and upper 13 cm is comprised of dark brown and dark gray silty clay.

Core 13

Core 13 is shorter (401 cm); the lithology is quite different from the other cores, yet some similar features are present. The bottom is filled with olive brown silty clay and sandy silt. From 393 cm a layer of olive silty clay is observed, having several layers of sand and yellowish-brown silt; clear sandy layers are seen at 323-321 and 339-335 cm. Above, olive brown and olive sandy silty clay is present, then it turns dark yellowish-brown at 317 cm. At 280 cm olive gray silty clay takes place, covered by olive brown and dark grayish brown mottled silty clay up to 264 cm. Very dark grayish-brown and olive gray silty clay is observed at 183-163 cm with a few coarser layers at 179-176 cm. Then yellowish brown sandy layers are seen at 163-161 cm, followed by brown and very dark grayish brown bioturbated silty clay till 141 cm. Above there are layers of slightly mottled light olive brown silty clay with some sand in the lower part. From 96 cm thin olive gray and very dark brown layers intercalate, replaced by a thick layer of dark brown and light olive brown alternations of silty clay and clayey silt. At 24-21 cm dark grayish brown sandy silty clay is seen. The top of the core is brown and light olive brown bioturbated silty clay becoming after 11 cm very dark grayish-brown silty clay.

4.2. Total Organic Carbon (TOC) content

Content of total organic carbon (TOC) is quite low in all three cores with a mean of about 0.2% (Fig. 5). In Core 11 it fluctuates from 0.1 to 0.67%, the numbers are high in the lower part of the core, where two prominent peaks of about 0.5% occur, and at the very top. In the middle part the content is relatively low and stable, though minor fluctuations are noticed. The TOC distribution in Core 12 is quite similar. The highest content of all cores (0.93%) is reached in a single peak at 610 cm. It looks smoother, but it is most probably due to a lower number of samples taken. Core 13 also has a peak of 0.5% at the surface. This core is distinctive with a lack of pronounced high in TOC content in the lower part, rather saw-shaped pattern is observed here, then above 300 cm the amplitude of fluctuations falls significantly.

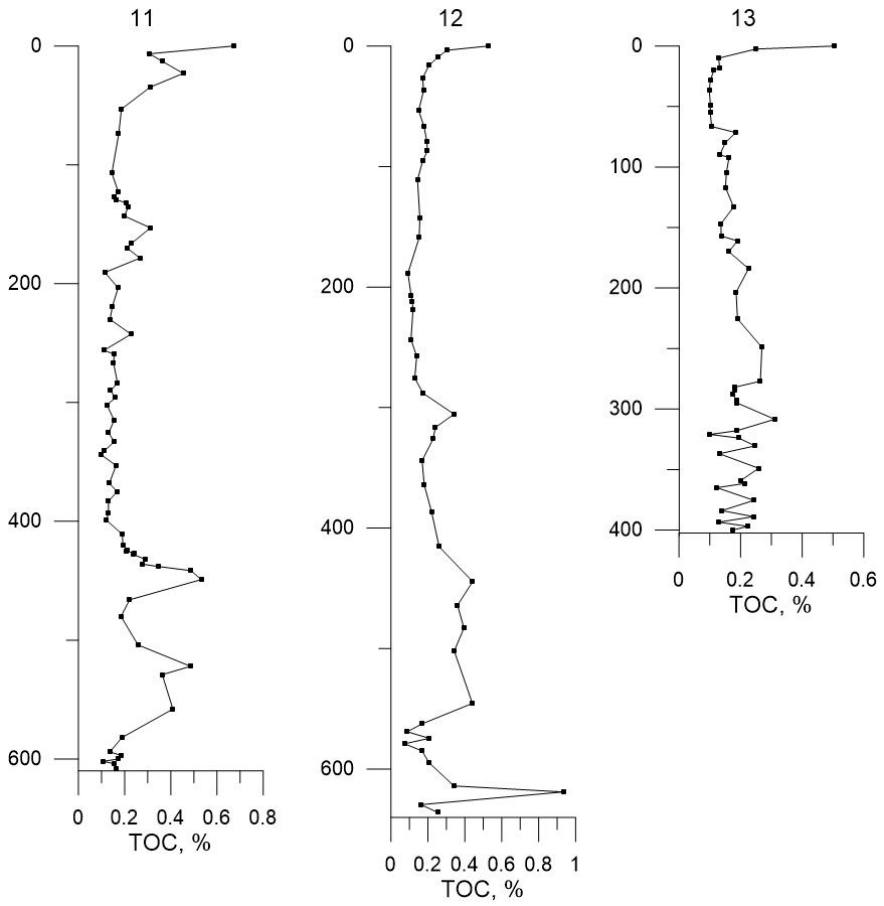

Figure 5. Total organic carbon distribution in the cores.

4.3. Fine fraction grain-size distribution

The compilation of grain-size distribution of the fine fraction (< 63 μm) in all samples is shown in Fig. 6. The cores demonstrate similar shape yet vary, mostly in amplitude. There is a small peak of 2% at about 5 μm and a higher one of 4-6% at 30-63 μm. In Core 11, fine particles comprise relatively high percentage while the coarse peak is narrower and lower than in the other cores. Just like in Core 11, Core 12 has a peak at 50 μm, though it is higher (up to 5.6%). The peak of fine silt is the least prominent in Core 13, but the amplitude is the largest. The coarse fraction peak is wide and includes finer fractions, unlike in other cores.

Such distribution indicates that the cores consist of layers with various grain-size, and the presence of very coarse silt is significant. Core 13 shows the highest diversity in sediments of different size.

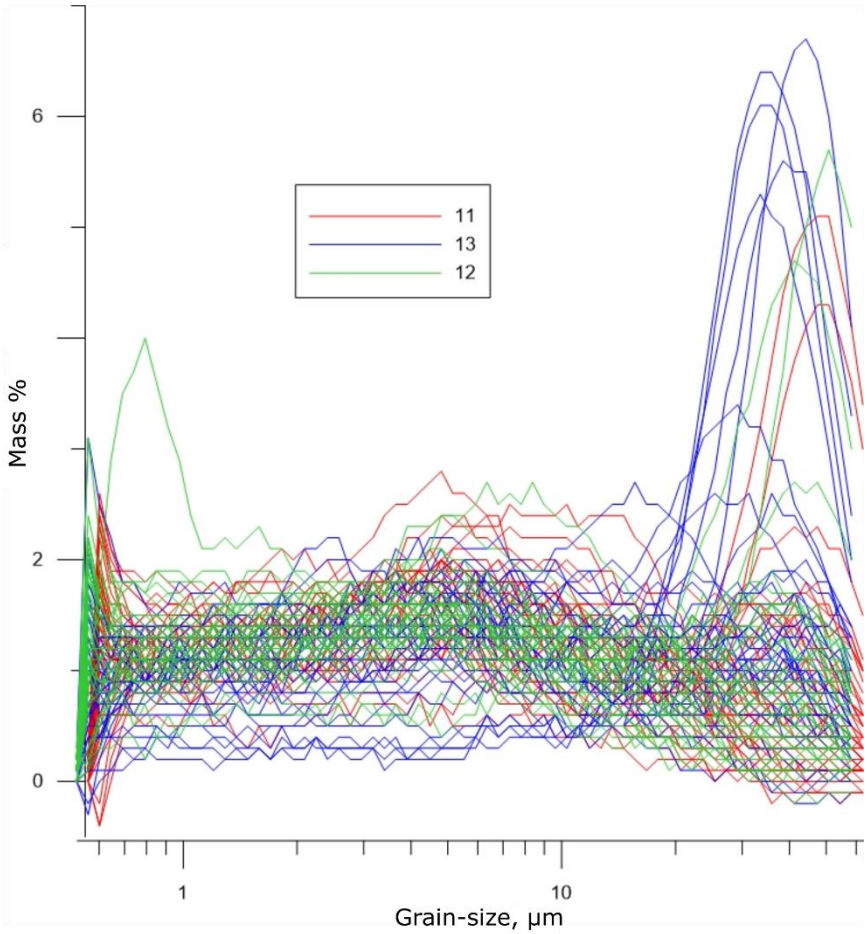

Figure 6. Mass percent grain-size distribution (fraction <63 µm) in the cores.

4.4. Grain-size fractions distribution

Detailed analysis of grain size allowed to study the distribution of particles of different sizes in the cores. Generalized Udden-Wentworth classification (Folk, 1957) was used (Table 1). As the research is concentrated on the study of paleo-current activity, the emphasis was made on the silt fraction as these are current-transportable particles (McCave et al., 1995).

Table 1. Grain size classification used in the study (Folk, 1957)

Fraction	Sand	Very coarse silt	Coarse silt	Medium silt	Fine silt	Very fine silt	Clay
Size, µm	>63	63-31	31-16	16-8	8-4	4-2	<2

A major part of all three cores is composed of clayey silt and silty clay (Fig. 7). Although, such types of sediments as silty sand and sandy silt are met as well in smaller quantities varying in every core.

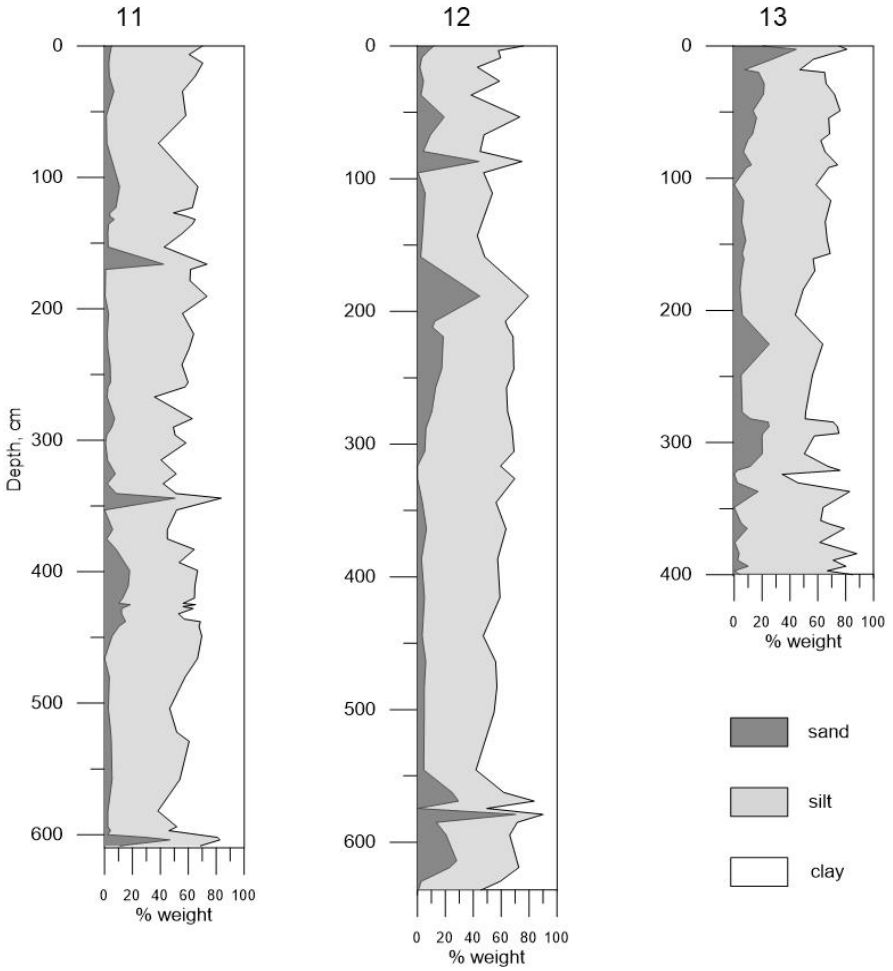

Figure 7. Sand, silt, and clay distribution in the cores.

Core 11

Core 11 is mainly composed of clayey silt with the silt fraction ranging from 31 to 73%; in 12 samples the amount of clay reaches up to 64%, so that silty clay is met. Silty sand is present in the core at depths 167-166, 345-344, and 605-604 cm, where sand comprises about half the percentage. Changes along the core are not dramatical, except noticeable sand content peaks which are accompanied by significant fall in clay. Yet in one case (167-166 cm) the clay fraction percentage stays at 26%, what can indicate bad sorting in the layer. Another example of a change is observed in clay and silt content: in the middle part of the core (440-120 cm) the period of fluctuation is much higher than above or below; the amplitude though is stable.

Core 12

The silt fraction again prevails in Core 12, fluctuating from 19.4 to 69.7%, so the sediments are clayey silt. Similarly to Core 11, silty clay is observed when clay content exceeds half the percentage and reaches up to 61.3%, what happens in 11 cases. In layers at 88-87, 189.5-

188.5 and 580-579 cm silty sand is present with a maximum sand content of 70.7% in the lower part, the amount of clay in this type of sediments is still quite high though. There is one sample at 570-569 cm where silt prevails, yet sand and not clay has a second great percentage, comprising sandy silt which is met only in this core.

The change of the sand fraction along the core is slightly different from that of Core 11: the mean amount of sand is larger (11% against 8% in case of Core 11), and peaks are not that sharp and are surrounded by smaller peaks. A saw-like pattern of silt and clay is seen here in the upper meter of the core. In general, the fluctuation of all grain-size fractions is in agreement.

Core 13

The dominating type of the sediment in Core 13 is again clayey silt with highly variable from 29.6 to 84.4% silt content. Silt reaches up to 65.5% in silty clay which is observed only in five samples. Silty sand is present in the core close to the top, at 2.5 cm, although the sand fraction here does not exceed silt greatly (44.6 against 36.3%). The fluctuation of grain size composition in this core is quite different. There are no clear highs in sand content, its distribution is more uniform, except for a single peak on the surface and two bulges at 320-200 cm. Changes in composition make high period fluctuations below 280 cm and chaotic low amplitude fluctuations above. Moreover, sand, silt, and clay are apparently less connected to each other, unlike in other cores.

4.5. Silt subfractions distribution

As it was mentioned before, the analysis of fine fraction composition is necessary for the study of current influence on the site. This is why the detailed information on the distribution of all subfractions of silt (very coarse, coarse, medium, fine, and very fine) is available.

Considering mean content and maximum and minimum values of all subfractions (Fig. 8), the character of distribution is quite similar in cores 11 and 12: the trend of mean percentage is fining with fine silt is peaking at 14% in Core 11 and 13% in Core 12, followed by very fine silt which has only 0.4% less in both cases. Coarse silt has the smallest mean value (about 5%) but the largest amplitude fluctuating from 0 to 28.6% and 26.7% in cores 11 and 12 respectively, what indicates its low content in general along with sharp coarse fraction peaks seen earlier in the sand record. These data support the description of cores 11 and 12 as fine in general with several coarser layers.

Core 13 has quite different characteristics. The mean content is approximately the same (10-11%) for every subfraction, which can point to the bad sorting in the core. Very coarse silt again has the largest variation, yet unlike in other cores, the maximum is leaning towards coarse particles reaching almost 47% in the coarsest part. This is the evidence for this core to contain the greatest amount of coarse material and to be in general less sorted comparing to the others.

Fig. 9 shows changes in the silt content along all cores; the percentage is recalculated so that 100% is a silt content in total. In all cores changes in very coarse silt are the most prominent, in Core 13 to a less extent though.

The fluctuations repeat the pattern of grain size fractions distribution: periods with high amplitude agree with such in Fig. 7. Apart from numerous coarse layers, coinciding with sand peaks, small short finings of sediments are clearly seen, for example, in core 11 at 427.5-426.5 cm and 128-127 cm, in core 12 at 326-325 cm. There is one case of an increasing amount of very fine silt up to 44% without major changes in the very coarse silt fraction at 268-267 cm in Core 11.

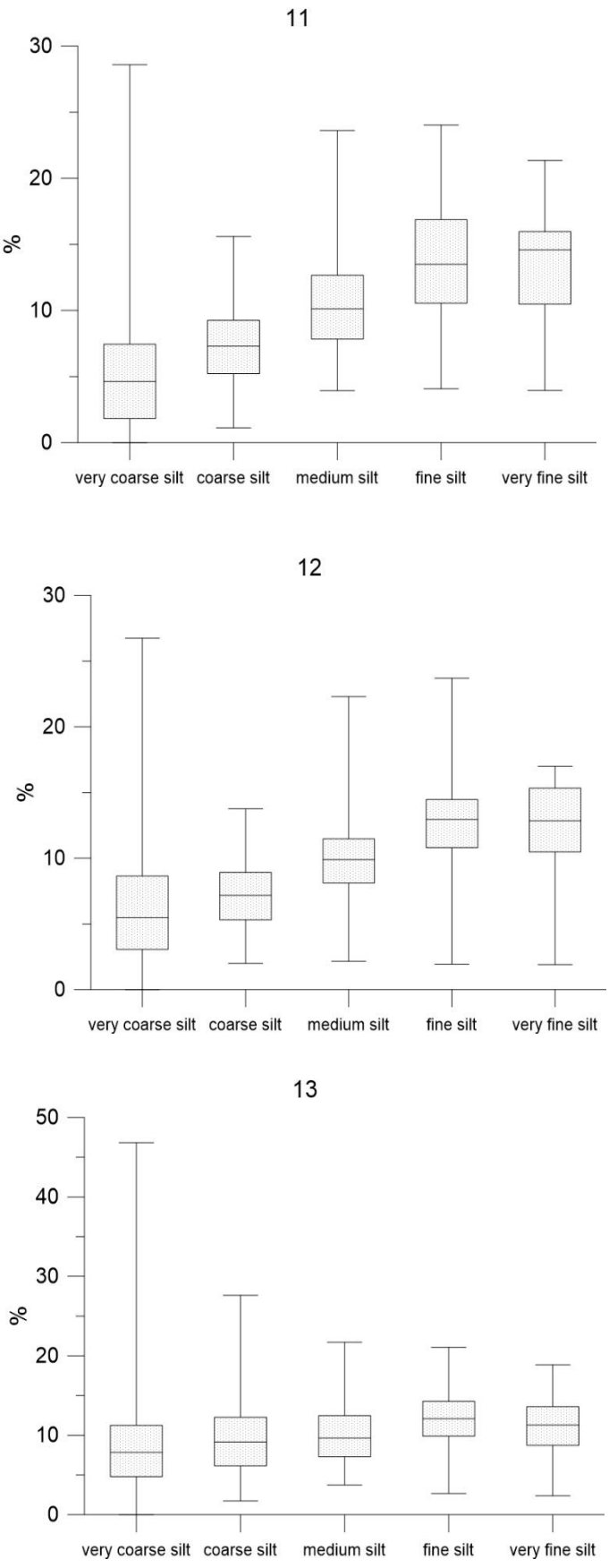

Figure 8. Box-whisker plots of silt subfractions in each core.

Such distribution demonstrates the dominating role of the fine fraction in the cores (fine silt and very fine silt) with high coarse peaks occurring rapidly, and only a few periods of finer material.

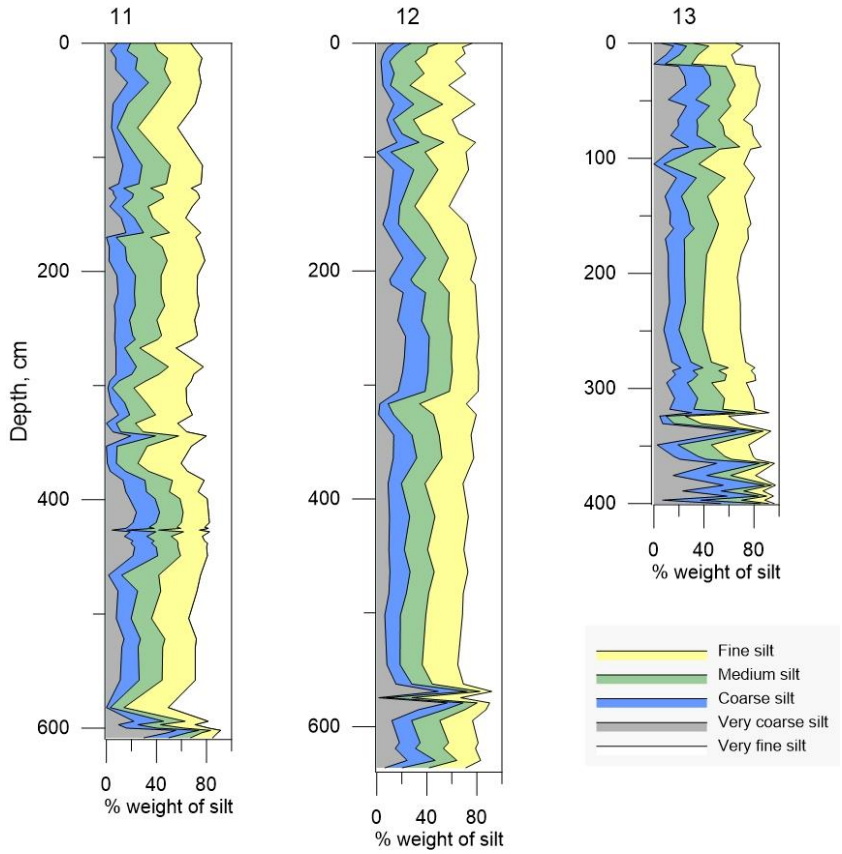

Figure 9. Distribution of subfractions of silt according to the classification by (Folk, 1957).

4.6. Sortable silt parameters

Being a major proxy for the strength of water circulation in the past, sortable silt mean ($\overline{SS}$, SS mean) as well as the percent of sortable silt (SS%) were subject to a detailed study. According to (McCave et al., 1995; McCave and Hall, 2006), a high correlation between these two parameters can indicate that sediments were current-sorted to such an extent that they hold a record of current speed.

The total content of $\overline{SS}$ and SS% (Fig. 10) varies in all cores. Comparison of mean $\overline{SS}$ gives a slight trend increasing towards Core 13: in Core 11 it is only 20.8 μm, in Core 12 – 22.3 μm, while in Core 13 – 24.3 μm, which again points to a coarser content of the latter core. Mean value is much closer to the minimum of about 14 μm in all cores than to the maxima of up to 43.5 μm in case of Core 12, indicating occasions of rare highs rather than a uniform

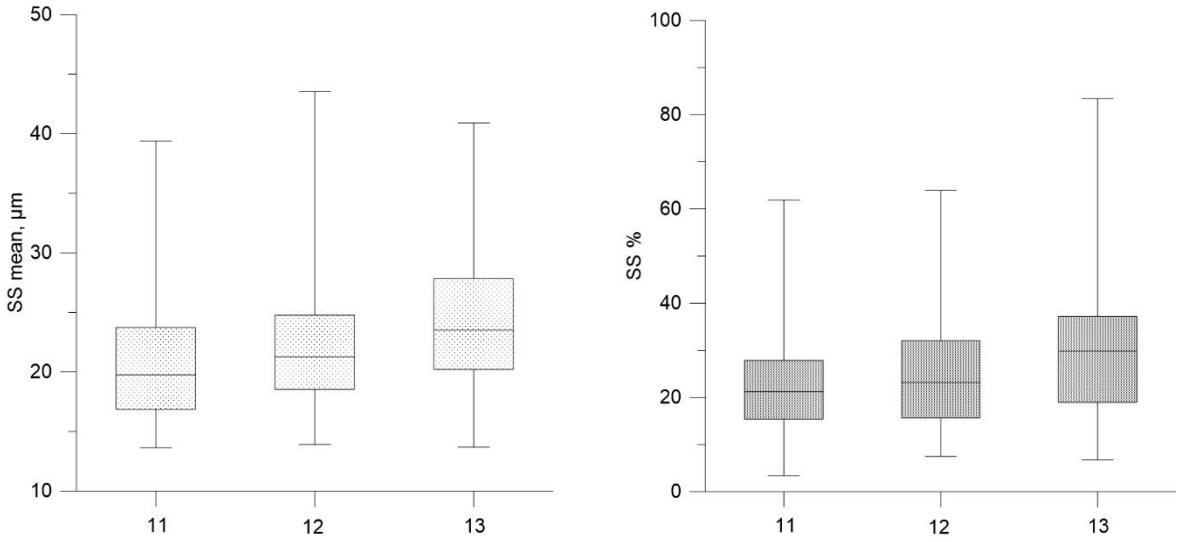

Figure 10. Box-whisker plots of $\overline{SS}$ and SS%.

distribution. Percentage of sortable silt fraction follows the same pattern, reaching 22.4% in Core 11 and 24.5% in Core 12 but 32.4% in Core 13.

Variation of the parameters along the cores (Fig. 11) is quite high in all cores. In Core 11, the sharp maximum is reached close to the bottom by both variables; above they fluctuate without a definite period. In general, the shape of the curves is similar, yet there are differences, for instance, at 280-260 and 200-150 cm. The correlation coefficient between the parameters is 0.83, which is quite high.

Despite the visually different shape of Core 12 curve, some patterns noted in core 11 are met here as well, including a section at 150-100 cm. The curves in this core are smoother, especially at depth 560-330 cm, what can be related to the flattest part of 11 core's curve (580-460 cm). The very bottom has, similarly to the Core 11 case, short high amplitude fluctuations. Above 300 cm variations seem more or less periodic with constant amplitude and a slightly decreasing trend towards the surface. The correlation coefficient is identical to that of core 11.

The curves of Core 13 seem outstanding first with their high amplitude and second with a lower connection between parameters (correlation coefficient is 0.78). Indeed, lower 100 cm are presented by high-periodic fluctuations. Above there is a low amplitude curve section up to 130 cm, distinctive with low correlation between $\overline{SS}$ and SS%; it corresponds to similar areas in other cores. Periodic fluctuations in the upper part are again stronger.

Basing on the information above, it can be concluded that $\overline{SS}$ fluctuates actively in each core from about 14 µm to slightly over 40 µm. Similar patterns allow correlating all three cores with each other, at least in the lower parts. Calculation of correlation coefficients indicates

a high role of currents in cores 11 and 12, and rather lower in Core 13. Although, as the coefficient was calculated for the whole record, and the curves reveal dynamics in the connection between parameters along the cores, there is a need in distinguishing the importance of current sorting in different parts of the cores.

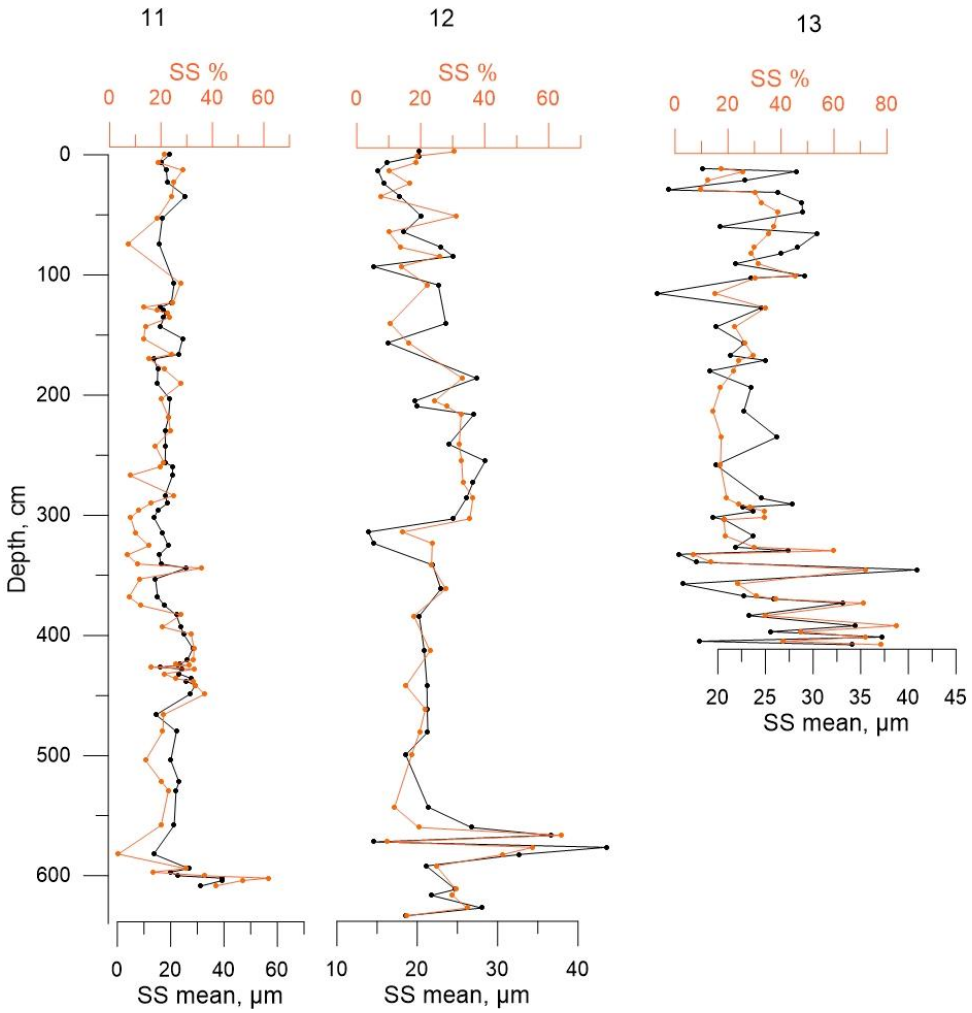

Figure 11. Calculated parameters percent of sortable silt (SS%) and sortable silt mean (SS mean).

4.7. Physical properties

In order to receive preliminary data about the cores and later create an age model, physical properties such as fractional porosity, p-wave velocity, wet bulk density (density) and volume-specific magnetic susceptibility (MS) were measured (F. Niessen/Stein, 2015, 2019). The latter two parameters proved to be sufficient for correlating of the cores with Core 109.

Both parameters fluctuate actively, forming patterns which are observed in each core (Fig. 12). Starting from the bottom, the first pattern is high amplitude fluctuations of density along with rising MS, for example, at 631-550 cm in Core 12 or 630-590 cm in Core 109. Above there is a peak in MS and a notable discrepancy between the parameters (570-500 cm in core 11, 290-130 cm in core 13). Then another peak in MS is seen followed again by divergence with prominent MS low (330-210 cm in Core 12, 120-60 cm in Core 13). Two higher peaks of both parameters and one low in between are observed in cores 109 (260-200 cm), 11 (200-160 cm), and 12 (110-80 cm). Then increasing trend of both parameters is seen (160-110 cm in Core 11), and then they go slightly down and stay stable. At the top, there is a decreasing trend for both MS and density after a small crest. Fluctuations in the upper part of Core 13 do not express any particular pattern, except for probably a peak at 1-0 cm.

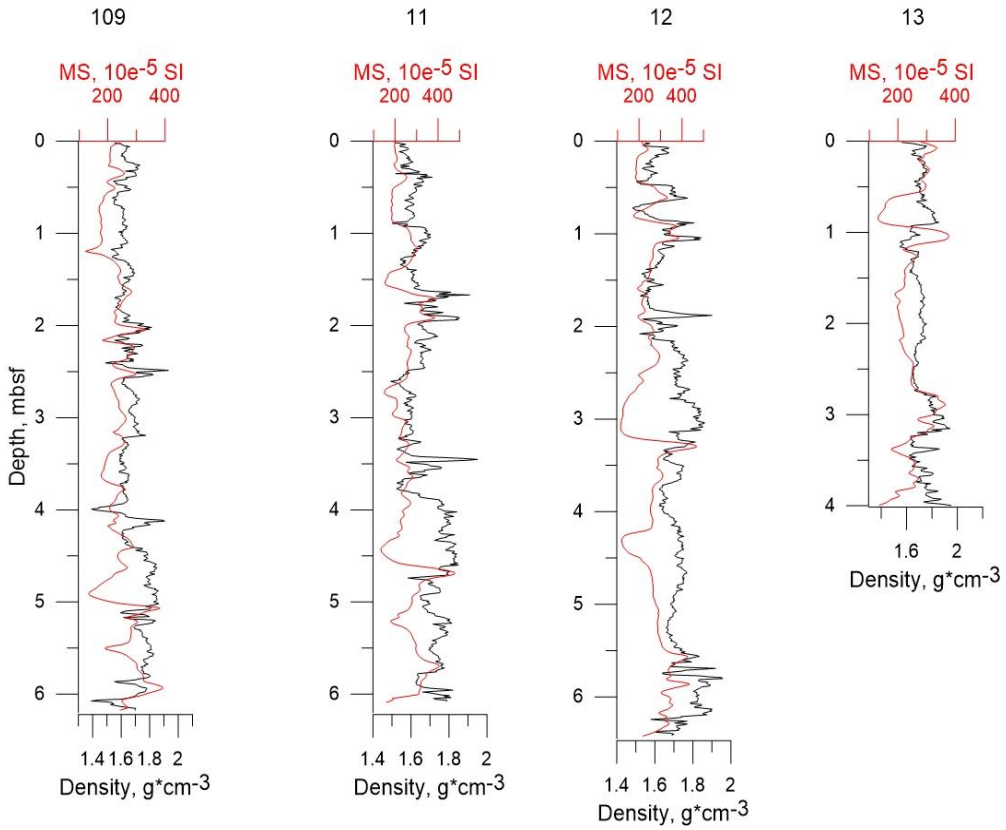

Figure 12. Wet bulk density and volume specific magnetic susceptibility for cores 11-13 (Stein, 2019) and 109 (Stein, 2015).

5. Discussion

5.1. Lithostratigraphy and age model

Paleoceanography studies reconstruct events that happened at some period in the past, therefore, proper age control is required here. As an absolute age determination was not performed for the cores in this study, the method applied here for dating is the correlation of the cores with the core with known ages of strata basing on their lithology and physical characteristics.

Results of the lithological description of the cores agree well with the general structure of sediments for the Arctic Ocean (Clark et al., 1980) describing them as a sequence of dark/brownish and grayish/olive layers. The brown layers are interpreted as sediments deposited during relatively warm periods (interglacial/interstadial), gray indicate periods with lower temperatures (glacial/stadial).

Along with lithological features, changes in physical characteristics were used to enhance precision in the determination of boundaries between the stages. As it was emphasized above, magnetic susceptibility and wet bulk density curves create patterns observed in all three cores.

The result of the correlation is shown in Fig. 23 (Stein, 2019). The data on Core 109 is taken from (Stein, 2015; Stein et al., 2017). First, Core 11 was related to Core 109 using physical properties curves, then patterns of both lithological features and physical properties characteristics in cores 12 and 13 were matched with those of Core 11 in order to determine the MIS boundaries in all cores.

The first unit from the bottom is characterized with presence of numerous sandy layers; there is a peak in MS which was used as a boundary between MIS 7 and 6 (190 ka) (all ages of MIS boundaries according to Lisiecki and Raymo, 2005). The part above contains prominent gray layers in cores 11 and 12 and olive layers in Core 13; it is bounded by a large minimum in MS considered to be the base of interglacial MIS 5 (130 ka). This part is very thick in all cores and marked with several brown layers including especially a big one in the upper part of cores 11 and 12. Two peaks of density and MS comprise MIS 4 (74-59 ka), what agrees with lithology as brown layers are absent here. The next unit is MIS 3 with thick brown layers; the upper boundary is a minimum in both physical properties (28 ka). Then there is plateau accompanied by a fine sediments unit with thin coarse layers, which is considered to

be MIS 2. It is followed by a short upward trend in physical properties indicating the start of MIS 1 (13.5 ka). The color is also darker here.

MIS 4, 3, and 2 were not present in Core 13. The assumption is that they were eroded by strong water flows or barely deposited for the same reason. Nevertheless, the sharp erosive contact was not noticed, probably due to bioturbation, so the boundary between MIS 5 and MIS 1 is less precise here than in other cores.

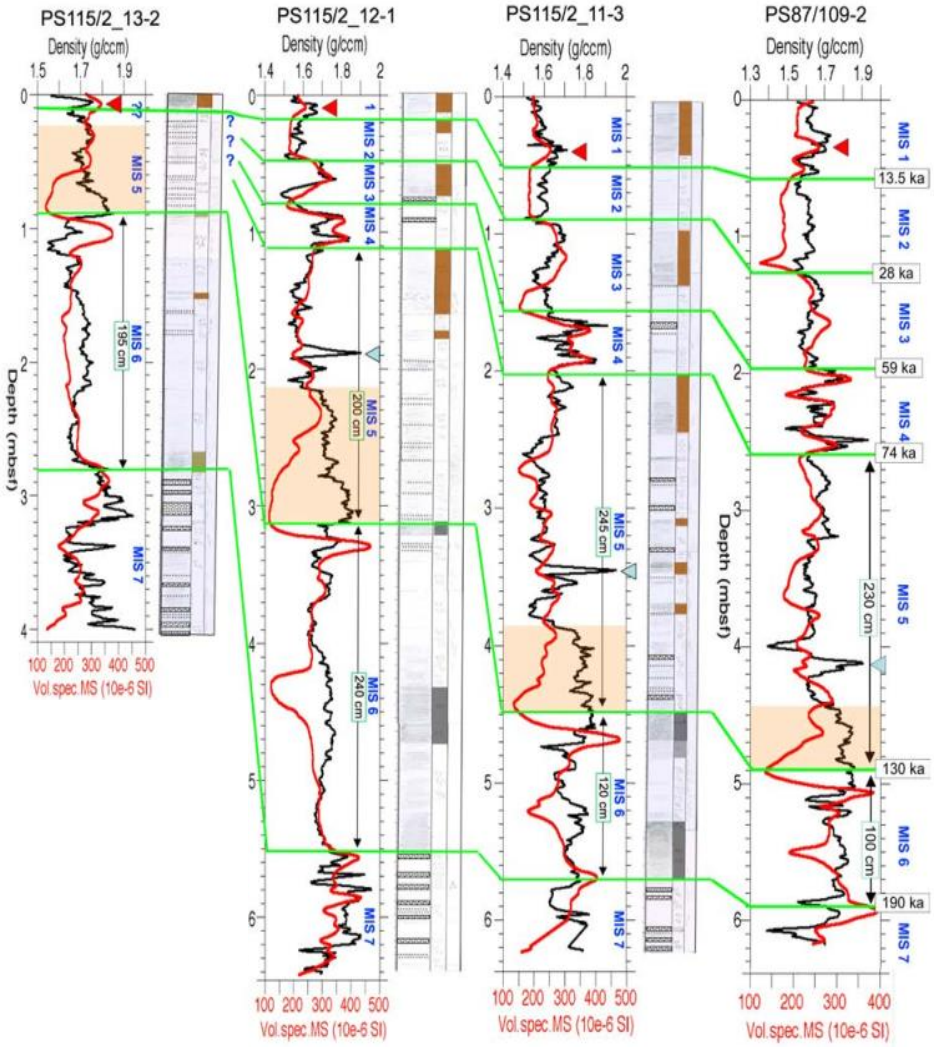

Figure 13. A preliminary age model with isotope stages MIS 7 to MIS 1, based on the correlation of cores 11, 12 and 13 to Core 109 and to each other using lithology and physical properties, is presented. Coarse-grained layers are indicated as dotted intervals. Intervals marked by light orange shading highlight lower MIS 5 including Termination II (Lototskaya and Ganssen, 1999; Moseley et al., 2015). Black numbers at the right are ages of MIS boundaries in ka = thousands of years BP (cf., Lisiecki and Raymo, 2005). The numbers surrounded by green rectangles are thicknesses (in centimetres) of the MIS 5 and MIS 6 intervals (Stein, 2019).

5.2. Sedimentation rate

Based on the boundaries of marine isotope stages, the linear sedimentation rates were calculated. The results are represented in Table 2 (cf., Stein, 2019). As the boundary between MIS 5 and MIS 1 is not determined precisely, the numbers for the sedimentation rates are rough.

Table 2. Sedimentation rates for the cores during MIS 6 to MIS 1 (in cm/ka^{-1}) (cf., Stein, 2019)

MIS/core	109	11	12	13
1	4.3	3.8	1.4	0.8
2	4.7	2.7	2.1	0
3	2.3	2.2	1	0
4	4.2	3.1	2.1	0
5	4.1	4.4	3.6	0.7
6	1.7	2	4	3.3

Figure 14. Age plotted against depth.

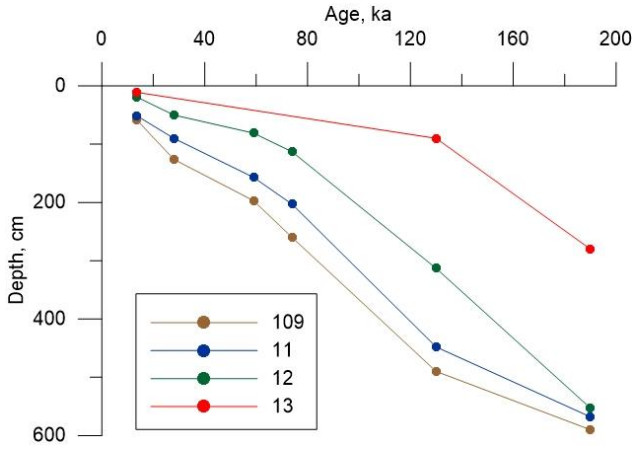

Table 2 and Fig. 14 reveal the general picture of sedimentation in a contourite system (Faugères and Mulder, 2011; Rebesco et al., 2014): higher sedimentation rates and active deposition are observed further away from the center of the channel and the current's main trajectory (Core 109 at the top of the drift and 11 on the lower flank of the channel), while in Core 13, taken from a bottom part of the channel, the sedimentation is limited, and a period of non-sedimentation or erosion is observed during MIS 4-2. As for changes in time, the sedimentation rates are relatively high during MIS 6-5 (especially in cores 12 and 13), then at about 70 ka (beginning of MIS 4) the curves become flatter meaning that sedimentation visibly reduced. That indicates more or less uniform deposition in all three cores in the first part of the studied period and change in the sedimentation mode later when the central area of the channel underwent scarce sedimentation and upper flank, on the contrary, gained more sediments.

5.3. Correlation coefficients for the fractions

Grain-size analysis proved that there is a general coarsening gradient from Core 11 to Core 13, that is from the outer part of the channel slope towards the central part. Apart from observing a total change in the coarse or fine fraction, there is a need in tracking the differences of the relation of fractions to each other, so that the most important components could be revealed. Moreover, high correlation between the fractions can indicate similar

nature of the transport process (Revel et al., 1996). In order to perform that, correlation coefficients for all fractions, $\overline{SS}$, and standard deviation, used as a measure of sorting (Revel et al., 1996), were calculated. Major meaningful ($p < 0.05$) positive connections are shown in Fig. 15.

In Core 11, very fine silt is tightly connected to fine silt, which in turn correlates with medium silt and sorting, which proves the dominating role of the connectionfine fraction in the core. Yet, clay is less significant here. Another cluster seems to have a totally opposite character: it is formed by coarser elements such as very coarse silt and sand, which slightly correlate with $\overline{SS}$. This is not expected as very coarse silt comprises particle with sizes 31-63 μm while mean $\overline{SS}$ for this core is only 20.8 μm, and the sand fraction supposedly consists of ice-rafted detritus to some extent. At the same time, the sand fraction has an insignificant negative correlation with the medium to very fine silt range.

The picture for Core 12 is alike, although there are several distinctive details. Clay is more connected here to very fine silt; the sand fraction correlates to $\overline{SS}$ even stronger than in Core 11 (correlation coefficient is 0.72 against 0.66), while the connection to very coarse silt is lost. Negative connection is met even for a larger number of silt subfractions, from coarse to very fine.

The connections in Core 13 are in general weaker. Only the compounds $\overline{SS}$–very coarse silt and fine silt–very fine silt remain stable. Here, sand does not correlate strongly positively with any fraction. The weak negative correlations are in turn observed with all silt-size particles.

One of the features in this sequence is the detachment of the sand fraction towards Core 13: it has less and less connection with other fractions. Accordingly, a number of negative bonds grows. This can indicate that the sorting is very bad, and presence of sand becomes more "unnatural", so apparently either the source of this fraction is discrepant, or the composition of the sediments has been altered as a result of some process.

According to (Hass, 2002), an assumption that the sand fraction is represented only by ice-rafted material and the main factor influencing the silt fraction accumulation is current-sorting requires minimal correlation between these two fractions. In the case of the current study, a correlation of the sand fraction with silt is negative and relatively large in Core 11, slightly stronger in Core 12, and the smallest in Core 13. Such a situation creates an implication that the coarse fraction is not necessarily ice-rafted and/or the silt fraction is not

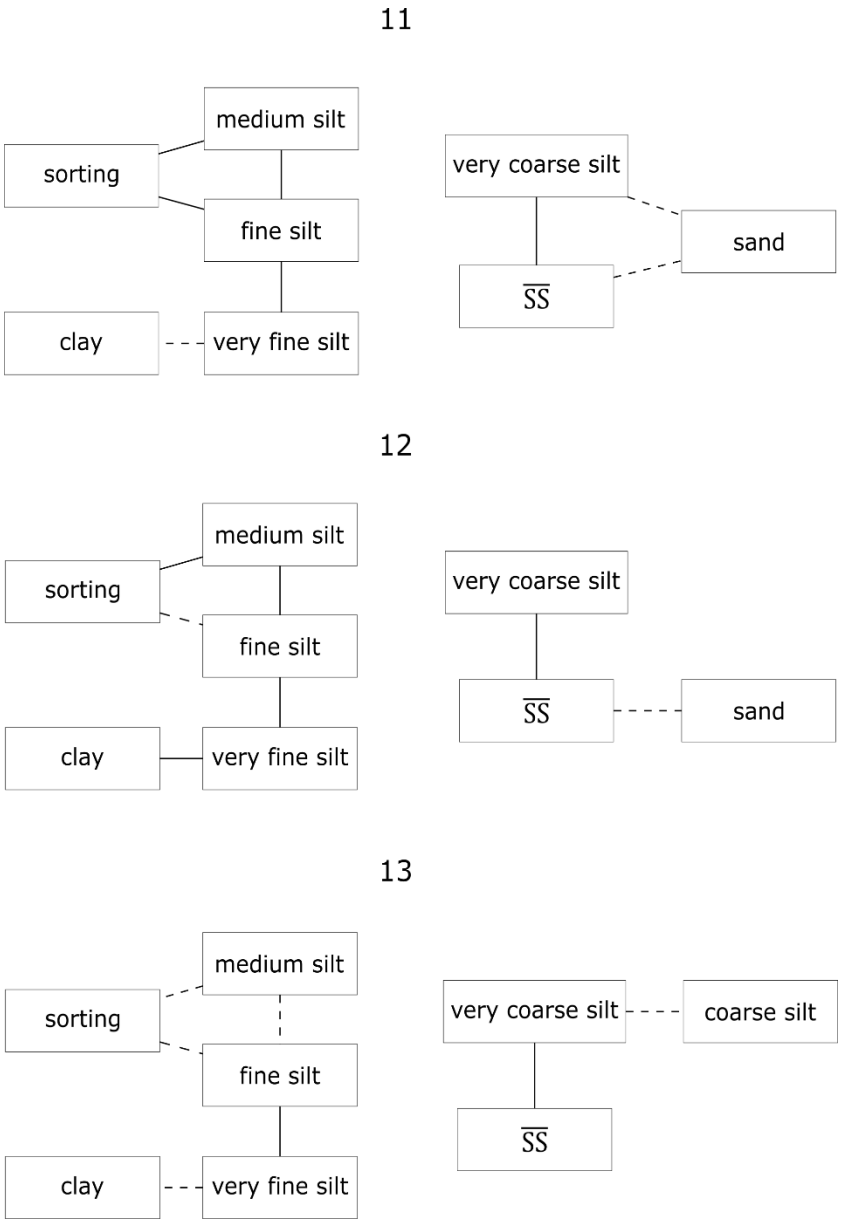

Figure 15. Connections between the fractions, sorting (standard deviation) and $\overline{SS}$ basing on correlation coefficients (solid line shows coefficients values 0.75-1, dashed – 0.5-0.75, the borders are based on a modified Chaddock's scale (Chaddock, 1925)).

current-sorted. Assuming that IRD input was equal in all cores as they are located quite close to each other, the changes in the silt fraction acquire more weight in the correlation. In Core 13 the correlation between sand and silt fractions is the smallest; thus, the silt fraction here was the most prone to current sorting. Stronger correlation in Core 12 points at a more active sorting here than in Core 11, which was placed higher on the channel flank. At the same time, presence of some correlation between sand and silt does not allow to consider sand to be composed of IRD only, though it can contain such particles (Hoffmann et al., 2019). Moreover, the periods of IRD deposition could just coincide with enhanced currents modes. Considering this, the attempts to eliminate the IRD effect should be taken with extreme care.

5.4. Moving downcore correlation and sortable silt mean record

It was proven that under a current's action, the sediments become well-sorted. Several attempts have been made to find a parameter that can estimate a measure of current sorting of the sediments. Some authors claim that positive correlation between $\overline{SS}$ and SS% is an indicator of sorting by currents (McCave et al., 2017). Use of the correlation between $\overline{SS}$ and SS% for this purpose gives satisfying results being applied to various data sets (Andrews et al., 2018; McCave and Andrews, 2019). Calculation of this parameter for the whole core can give an estimation of how much it was affected by currents, and gives an opportunity to compare it with other cores in different locations.

Although, the environment and factors of sedimentation mode change with time even in one point, what created a need in the estimation of sorting by currents in different parts or along a core. One of the possible ways to do that is to calculate a correlation coefficient separately for each MIS. Considering different sedimentation rates during every period, the number of samples varies significantly, making such an analysis not very reliable. The solution to this might be the calculation of running (moving) downcore correlation coefficient, which creates a continuous record of correlation between $\overline{SS}$ and SS% (McCave and Andrews, 2019). It allows to compare sorting in segments of a core and discover when the currents reworked the sediments most and when their influence was not that great. The window of correlating points was chosen basing on the length of the cores, sampling resolution and shape of a graph, which should be neither too smooth nor have too high amplitude of fluctuation.

At the same time, considering $\overline{SS}$ alone to be a parameter sufficient to indicate currents influence, the correlation between $\overline{SS}$ and SS% can be used as a factor determining whether it is appropriate to use $\overline{SS}$ as a current speed indicator or not. As a result of calculations, coefficient of 0.5 was suggested to be used as a borderline, making $\overline{SS}$ a proxy of currents action not applicable in the segments of the cores where the correlation coefficient is less than 0.5.

Fig. 16 shows the running correlation coefficient in cores 11, 12, and 13. Several runs with various windows proved 7 points to be the optimal width. The results vary in all cores. One whole part from the end of MIS 5 to the beginning of MIS 2 showed a low correlation in Core 11. Glacial periods were to the most extent subject to a low correlation in Core 12, although the parameter fluctuates actively during MIS 6 and 5, and is very close to 0.5 during

MIS 3. During both MIS 6 and 5 in Core 13, the correlation tends to zero and below, yet in between there is a part with very high correlation.

Basing on that, MIS 7 proved to be the most stable in means of a high correlation between $\overline{SS}$ and SS%, indicating the highest degree of sorting by currents. MIS 6 shows a decreasing trend from Core 11 to Core 13: in the first one the correlation is not too high yet above 0.5, in Core 12 it drops to zero twice, in Core 13 the coefficient is below 0.5 at the beginning of MIS, but at the end it rises high. The shape of the graph during MIS 5 looks quite similar in the cores: it is high at the beginning of the period and then gradually decreases. In Core 13 there is a high at the end of this MIS, but it is necessary to consider that the boundary between MIS 5 and 1 here is not very accurate. Low correlation is observed in MIS 4 in both cores where this period is present; the same is applicable for MIS 3, though the coefficient is higher in Core 12. There is a low in Core 12 during MIS 2, but in Core 11 the correlation is, on the contrary, peaking. The correlation coefficient is above 0.5 in all cores during MIS 1, although unlike Core 11, where it decreases in time, in cores 12 and 13 it increases.

Such a comparison makes an implication of different extent of current sorting varying with time in each core, what is seen clear, especially in MIS 6. There is a need to notice that, as it was mentioned before, sampling resolution varied in all cores and along a core; therefore, a number of samples per MIS varied significantly making a comparison rather rough, particularly in parts MIS 4-1 with a quite low sedimentation rate. Nevertheless, such an analysis can be and was applied to accompany the record of $\overline{SS}$ in order to evaluate the reliability of this parameter. Segments of the cores with a low correlation between $\overline{SS}$ and SS% were not excluded from the further analysis of $\overline{SS}$, yet the evidence of such a low possible current sorting was considered. Fig. 17 shows $\overline{SS}$ records which include running downcore correlation data to emphasize the periods when the sediments were less affected by the currents.

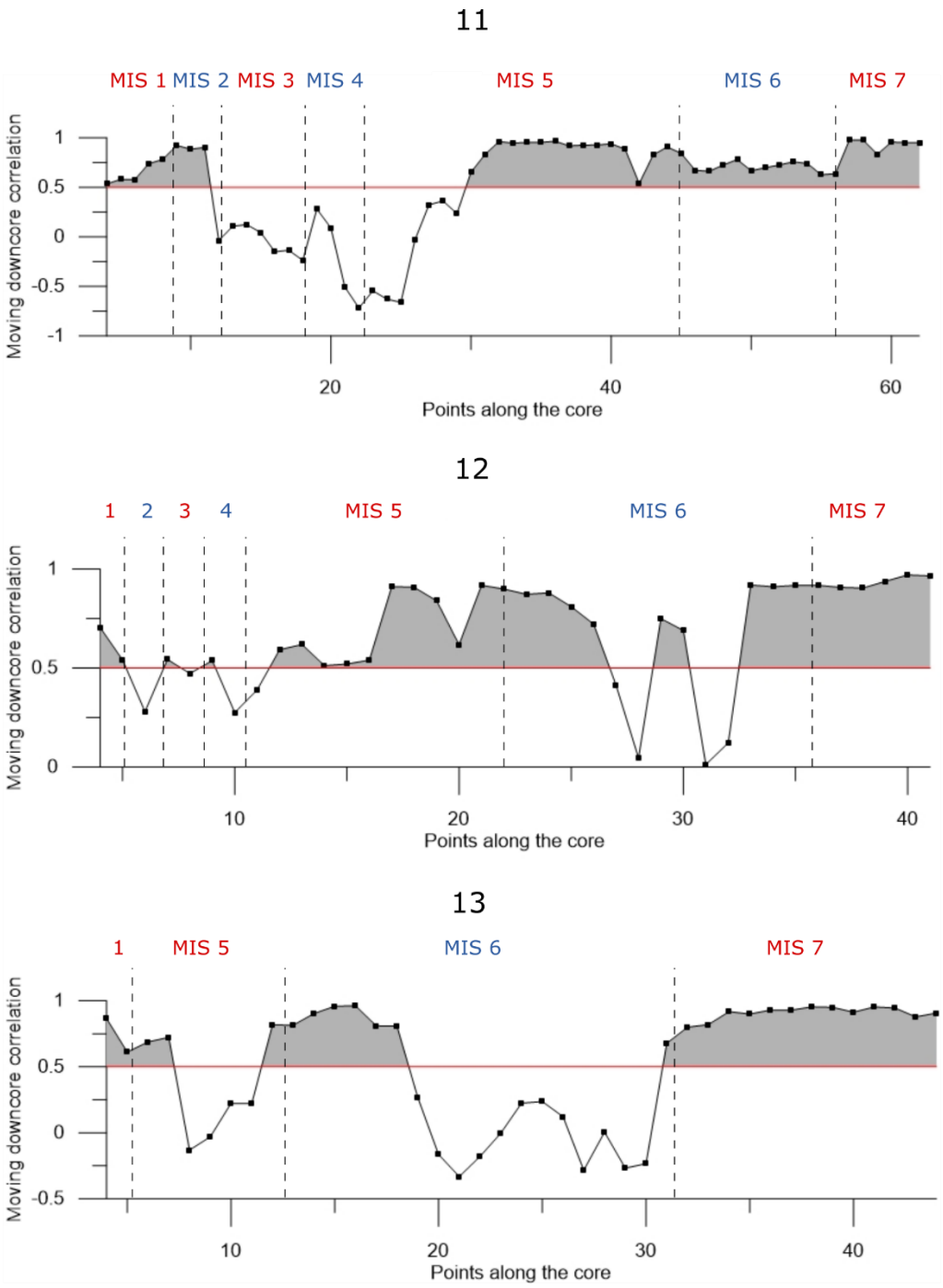

Figure 16. Running downcore correlation between $\overline{SS}$ and SS%, the areas with gray shading indicate correlation coefficient > 0.5.

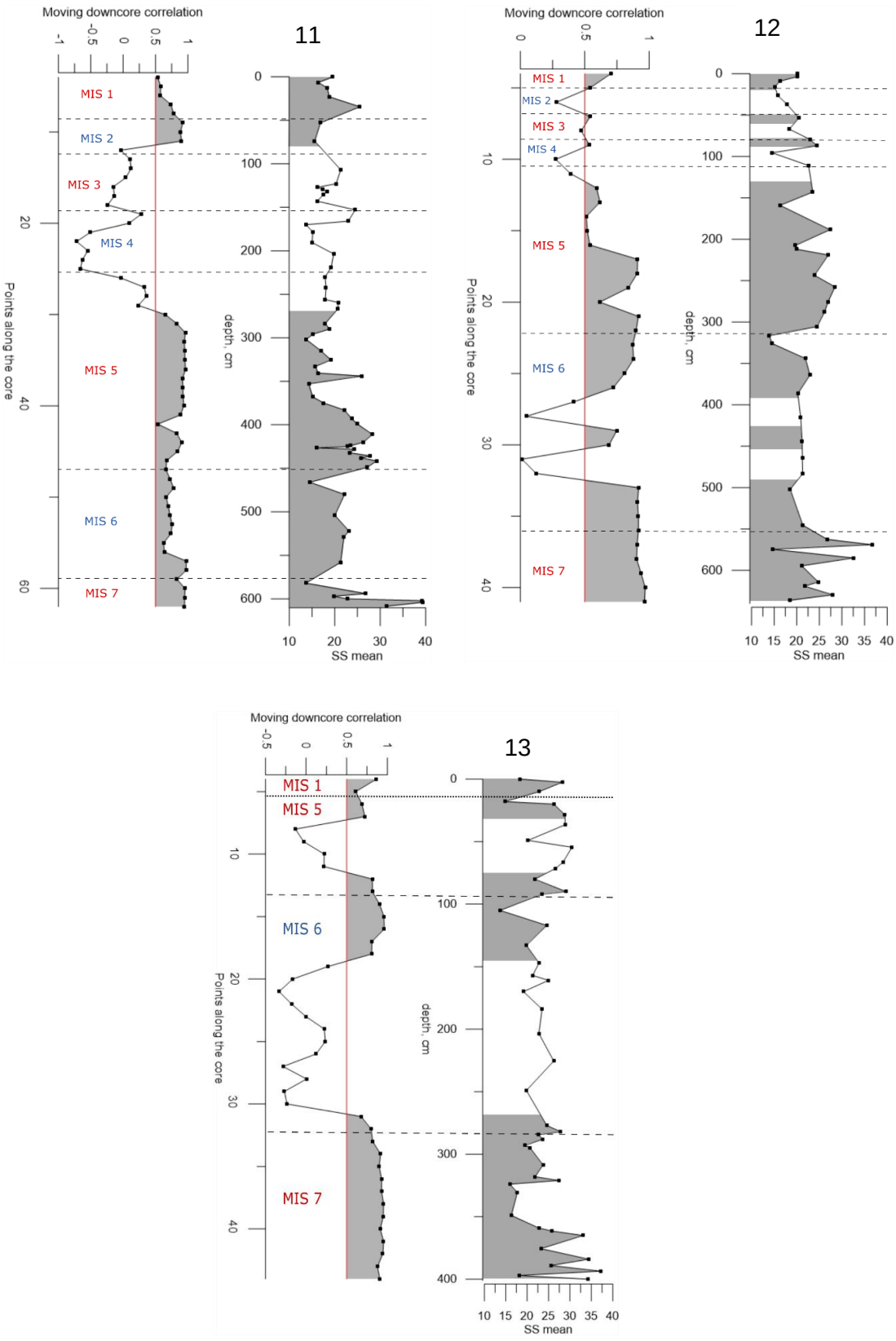

Figure 17. Running downcore correlation with the $\overline{SS}$ record.

Sortable silt mean record (Fig. 18) in Core 11 shows high peaks corresponding mostly to transitional phases or interglacials: high numbers (above 25 μm) are reached during MIS 7, at the beginning and middle of MIS 5 and the beginning of MIS 1 as well as at the transition of MIS 4 to MIS 3, though downcore correlation does not indicate $\overline{SS}$ during this period as current-sorted. All the peaks in Core 12 repeat the picture for Core 11. Resolution of MIS 7 is higher here so that high amplitude fluctuations are seen. Core 13 is notable with higher amplitude and period of fluctuation, especially in MIS 7 and MIS 5, which indicates very strong flow during interglacials and rapid changes in speed. The preliminary age model for this core indicated extremely low sedimentation rate during MIS 4-2, the reason for this is most probably a too high speed of flow for the particles to deposit or even erosion during the period of a strong current, although no sharp contact was found. Bad current-sorting is suspected in a great part of MIS 6. The middle part of MIS 5 is supposedly also not current-affected as the correlation between $\overline{SS}$ and SS% is quite low. This period is marked with several climate changes and events, so changes in speed of currents could correlate with them.

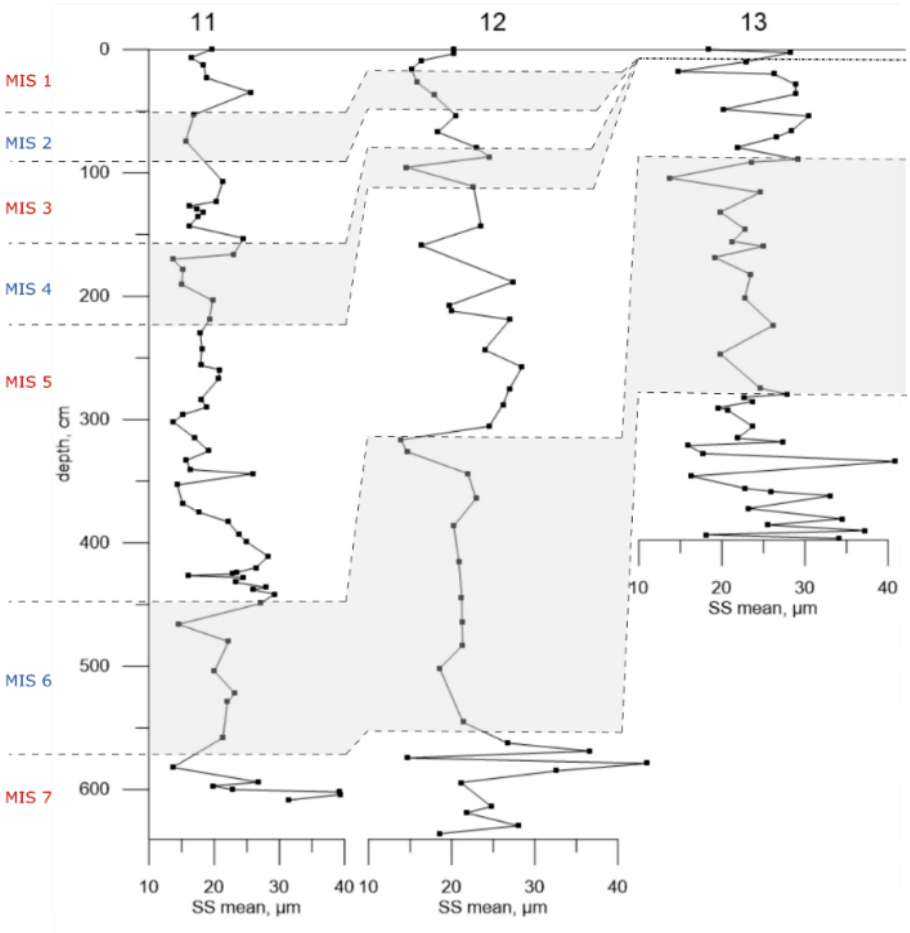

Figure 18. Distribution of $\overline{SS}$ in the cores; glacial periods are shaded gray.

Comparison of the numbers for $\overline{SS}$ with the published data from different areas proves the sorting in this study to have both significant strength and high amplitude. $\overline{SS}$ in this study fluctuates from 14 to 40 μm while for example in the North Atlantic it changes only from 16 to 25 μm (Jonkers et al., 2015), in the South China Sea from 16 to 23 μm (Li et al., 2017) and 14 to 21 μm in the Labrador Sea (Hoffmann et al., 2019). Only $\overline{SS}$ record from the Drake Passage reaches close: 16-37 μm (Lamy et al., 2015), what, considering the power of water going through the Passage, evidences reasonably strong currents in a channel on southern Lomonosov Ridge.

5.5. Elimination of IRD effect

As the study area is located close to the North Pole, it is surrounded by places of iceberg formation as well as seasonally and perennially covered with the sea ice (Obrochta et al., 2014; Stroeve and Notz, 2018). Both these factors of ice presence in the ocean influence sedimentation character as floating ice can be a source and transport agent of sediments. Being a solid substance, the ice floes, unlike sediment transport within the water mass, may entrain and transport large and heavy particles, and deposit them after melting. The terrigenous particles which were transported and deposited to the bottom of the ocean are called “ice-rafted debris (detritus)” or IRD (e.g., Bischof et al., 1996; Darby et al., 1997). Therefore, a presence of coarse-grain sediments in the core from high latitudes quite often indicates a presence of ice there. At the same time, the activity of strong currents can cause winnowing and lead to a formation of coarser layers, not to mention that sometimes currents can carry particles larger than clay and silt (Lamy et al., 2015). At the same time, silt can be carried by the ice too, and in great amounts. This poses a problem of distinction of one source of coarsening from another while trying to estimate a degree of current sorting in an Arctic core.

There have been several attempts to distinguish and/or eliminate IRD in sediments, for example, using end-member modeling (e.g., Jonkers et al., 2015; Hoffmann et al., 2019; Wang et al., 2018). Some authors though claim this analysis to be ineffective for the ice effect elimination in current-sorted sediments (McCave and Andrews, 2019). Another approach is taking the whole sand fraction as ice-rafted due to the implication that such large and heavy particles cannot be transported by currents (Hoffmann et al., 2019) and then using deviations from a regression function created by plotting the sand fraction content against $\overline{SS}$ (Hass, 2002). Fig. 19 shows such graphs and equations for each core. The function describes the correlation between the sand fraction and $\overline{SS}$. Samples which lie on the

regression line were deposited under “average” conditions when IRD variations were not high, while scattering around the line indicates moved equilibrium with either high IRD input or strong current sorting.

Inserting sand content into the equation as *x* allows to calculate potential $\overline{SS}$ ($\overline{SS}_{pot}$) supposedly showing the $\overline{SS}$ record without current influence. Subtraction of $\overline{SS}_{pot}$ from $\overline{SS}$ gives the so-called delta $\overline{SS}$ – the equivalent of $\overline{SS}$, only without IRD influence. There is a need to notice that during the current study no measurement of the upper limit of sand was made. Based on visual observation, 2 mm were used as the borderline.

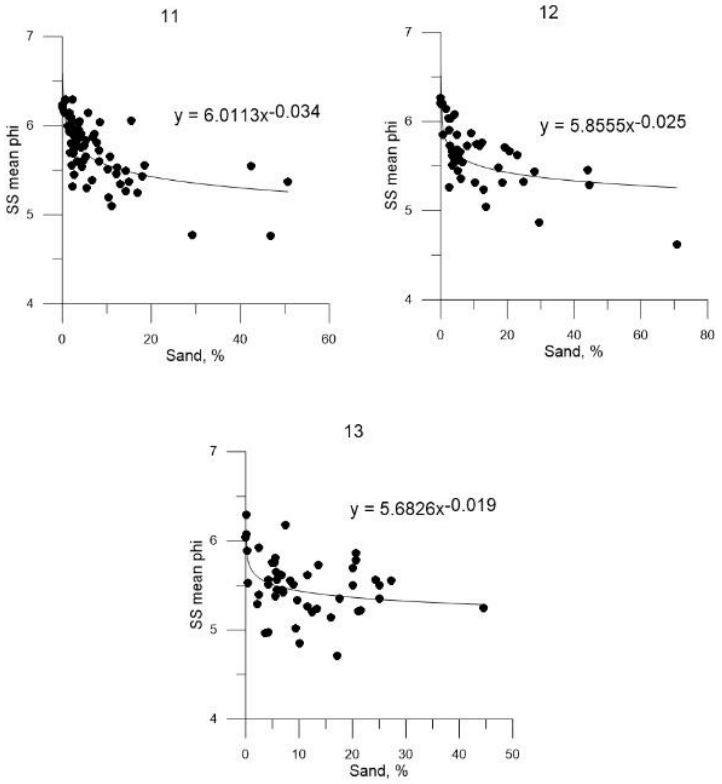

Figure 19. $\overline{SS}$ in phi scale plotted against sand percentage, and a trend line.

The results of the calculations for every core are shown in Fig. 20. In all cores, the curve of delta $\overline{SS}$ has absolutely the same shape as $\overline{SS}$, only with slightly higher amplitude and a few (4-5) μm lower. $\overline{SS}_{pot}$ fluctuates only within 0.79-1.33 μm. In order to compare delta $\overline{SS}$ and $\overline{SS}_{pot}$, the ratios of their variances were calculated. In Core 11 this parameter equals 8.5, in Core 12 it is 7.9 while in Core 13 – 10.4, what indicates that major part of the silt fraction fluctuation is current-induced and to a higher extent in Core 13. Surprisingly, the ratio in Core 12 is somewhat lower than in Core 11. Considering that the variance of delta $\overline{SS}$ is gradually falling towards the bottom of the channel (from 0.37 through 0.36 to 0.3), the reason is a higher $\overline{SS}_{pot}$ variance in Core 12 (0.05 against 0.04 in Core 11). Therefore, such

calculations do not agree with the assumption that IRD input was the same in all cores which is unrealistic. Although, high variation of the coarse fraction does not necessarily mean increased or reduced IRD input in one particular core.

Several small peaks in $\overline{SS}_{pot}$ (it is given in phi-scale, so smaller numbers mean greater size) were noticed in all cores' records. They are in general coincide with sand peaks. A fall and then a sharp rise was observed during MIS 4 in cores 11 and 12. This peak could be a true IRD-rich layer, as the deglaciation phase is accompanied by active icebergs movement in the ocean, which then melt as the temperature rises; according to the studies (e.g., Svendsen et al., 2004), Eurasia experienced the glaciation covering probably even Severnaya Zemlya archipelago at the end of MIS 4, so that the glacier was the closest to the studied area. The peaks almost always follow more prominent lows. Some of the lows are though individual, for example, at the end of MIS 6 in all cores, coinciding with low delta $\overline{SS}$. Cores 12 and 13 have smaller falls at the end of MIS 7, which probably might be found in Core 11 has it longer recovery of this period. Core 11 has another fall and rise in the middle of MIS 5, most probably reflecting another IRD input during the end of one of the glacial sub-stages, such as 5b (the precise age is hard to determine using current age model) (Spielhagen et al., 2004).

Considering that $\overline{SS}_{pot}$ presumably shows sortable silt fluctuation as it would be without current-sorting, very flat and smooth distribution of this parameter in all cores demonstrated the dominant role of currents as a sedimentation factor in the area, while delta $\overline{SS}$ repeating $\overline{SS}$ pattern only supports this. Unfortunately, the precise size range of the sand fraction was not determined; this fact could influence on the calculations, leading to artifacts. Also, considering that the sand fraction can be current-sorted as well as transported by the ice while here all particles larger than 63 μm are considered to be IRD, the results of distinguishing between IRD and current-sorted material require closer study using probably some other techniques. The main feature that distinguishes current-influenced material from all other types is still good sorting, that is why it should be used as a current activity indicator.

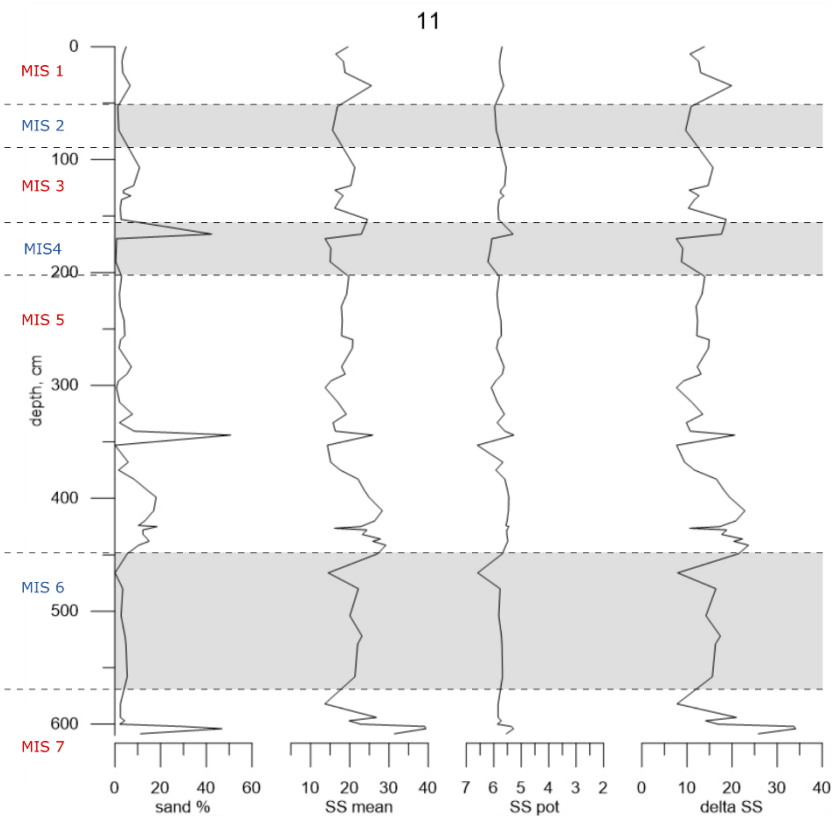
11
MIS 1
MIS 2
MIS 3
MIS4
MIS 5
MIS 6
MIS 7
depth, cm
0
100
200
300
400
500
600
0 20 40 60
sand %
10 20 30 40
SS mean
7 6 5 4 3 2
SS pot
0 10 20 30 40
delta SS

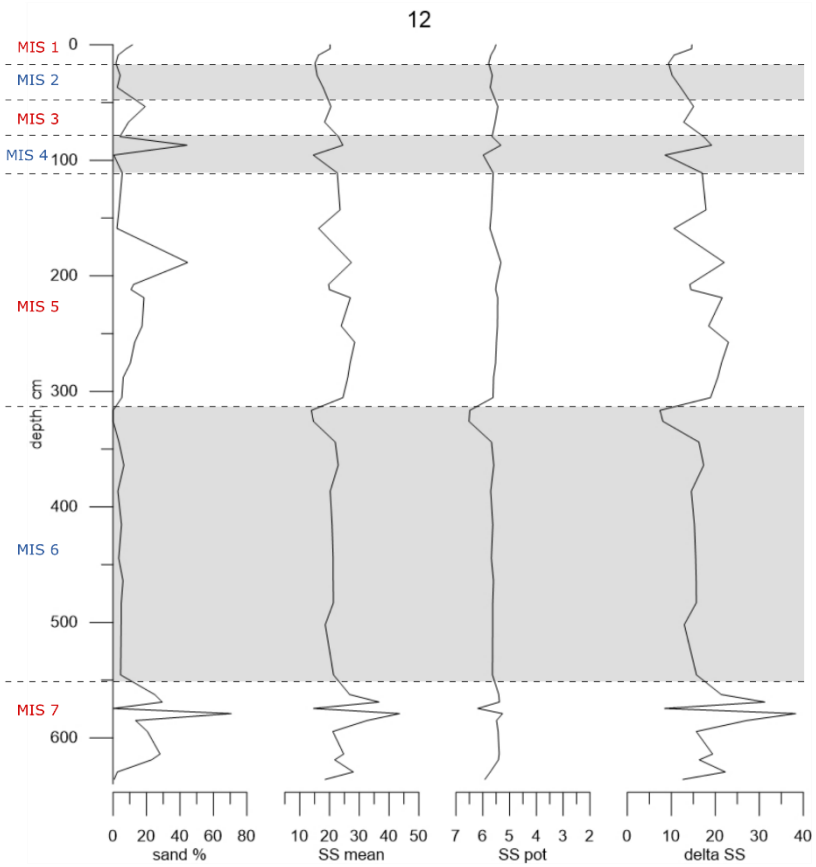
12
MIS 1
MIS 2
MIS 3
MIS 4
MIS 5
MIS 6
MIS 7
depth, cm
0
100
200
300
400
500
600
0 20 40 60 80
sand %
10 20 30 40 50
SS mean
7 6 5 4 3 2
SS pot
0 10 20 30 40
delta SS

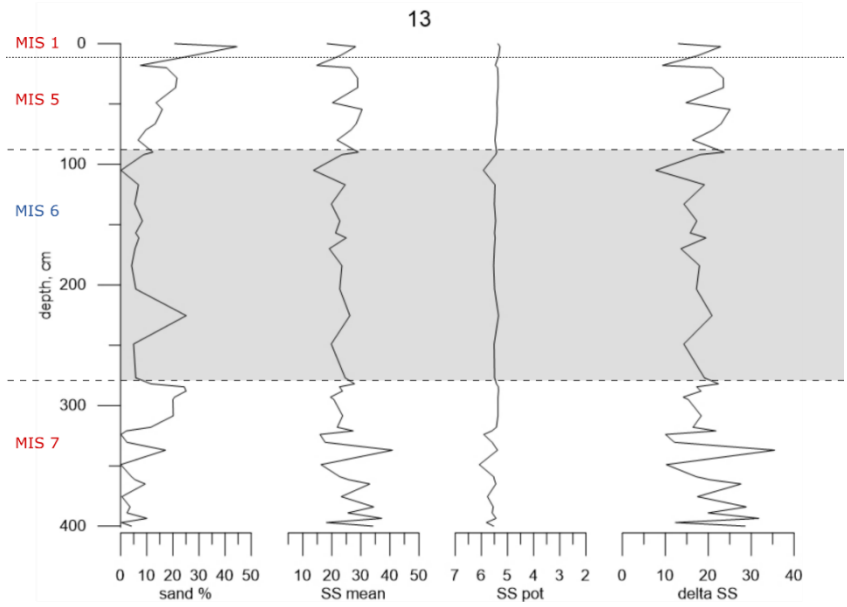

Figure 20. Sand percentage, $\overline{SS}$, potential $\overline{SS}$ and delta $\overline{SS}$ in the cores.

5.6. Cluster analysis

K-means cluster analysis was performed using the following parameters: TOC, SS%, $\overline{SS}$, sorting (standard deviation), $\overline{SS}_{pot}$, delta $\overline{SS}$, wet bulk density, magnetic susceptibility, the content of sand, very coarse silt, coarse silt, medium silt, fine silt, very fine silt, and clay. An optimal number of clusters was six (Fig. 21), despite some of them intersect.

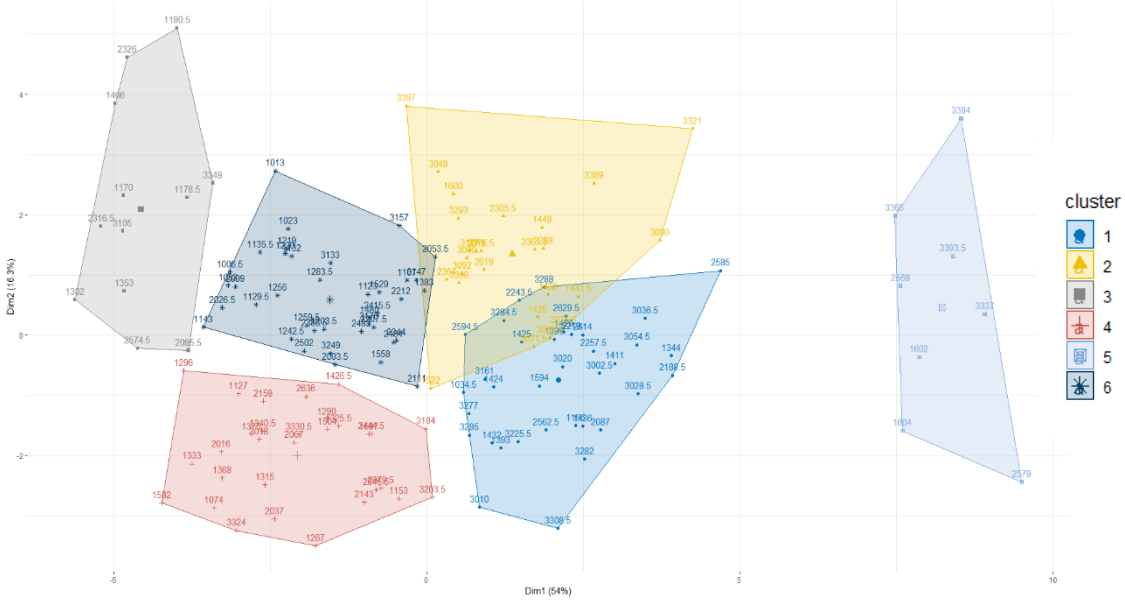

Figure 21. Cluster plot of all samples.

Each cluster had its combination of characteristics; the most distinctive are represented in Table 3. The evaluation was based on distribution of the parameters: mean, minimum and maximum values; grain-size column summarizes all grain-size fractions data.

Table 3. Characteristics of clusters (color scale does not match that of Fig. 21)

Cluster	TOC	Grain-size	SS mean	Sorting	Density
1	middle	clayey sand	middle	very good	middle
2	high	coarse silt	middle	middle	high
3	middle	fine silt	very low	very bad	low
4	middle	silty clay	very low	very good	very low
5	low	silty sand	very high	very good	very high
6	high	fine silt	low	bad	very low

Plotting clusters in the cores with the developed earlier age model (Fig. 22) proved the quality of the age model as in general each MIS had its distinctive sequence of layers; the glacial and interglacial periods also have different features. The goal of this analysis was to classify all samples basing on the known information at the same time grouping them, and particularly to determine the period when the accumulation in Core 13 was scarce, or erosion happened. Every sample was considered here so that a high-resolution record was created.

MIS 7 is the only period when sediments of cluster 5 are present in all cores. They are the coarsest, the densest, current-sorted and poor in TOC, indicating the strongest water flow impulses. These sediments are combined with clusters 1, 2, 3 and 4, in Core 12 presence of cluster 1 is more prominent. This is some kind of a transitional type considering its mixed grain-size yet good sorting. In Core 13 sandy layers intervene with dense rich in organics coarse silt of cluster 2, indicating lower energy of the environment.

MIS 6 looks similar in cores 11 and 12: cluster 6 of low density rich in TOC bad-sorted fine silt with an indication of low current influence dominates. There are more of cluster 1 sediments in Core 13 in this period so that no sharp boundary is seen between MIS 7 and 6. It could be due to mixing during some small-scale mass-wasting processes or bioturbation. Similarly to MIS 7, layers of cluster 4 are observed here, only in larger amount. These sediments are very fine in grain-size and have low $\overline{SS}$ meaning that no strong current action happened there at that time. In all three cores, this period ends with sediments belonging to the cluster 3, which represents very bad-sorted fine silt with no evidence of increased current's speed. The composition agrees with the glacial period's environment during which

the cluster is seen: IRD input explains bad sorting, and weaker water stream reduces current sorting.

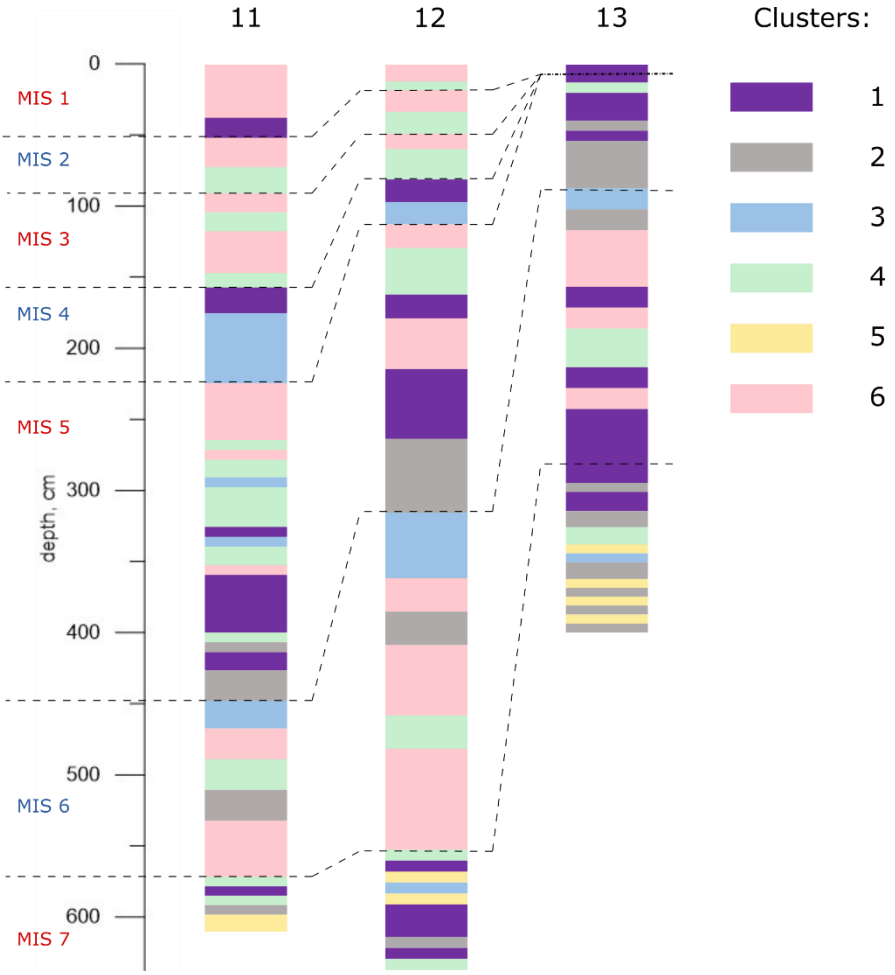

Figure 22. The cores divided into 6 clusters.

MIS 5 is represented by various clusters combination depending on sampling resolution and sedimentation rate in the core. This situation reflects numerous climate changes during this period (Oppo at al., 2001). It starts with a layer of cluster 2 and transforms to cluster 1, indicating a period of intermediate current influence. Then in cores 11 and 12 clusters 4 and 6 dominate evidencing a slow-down till the beginning of the MIS 4. The upper part of MIS 5 in Core 13 is different: it is built with sediments of mixed type, spreading to the surface.

MIS 4 is the most easily distinguished glacial period. It contains sediments of cluster 3, typical for the cold period, and 1, which is characteristic for transitional periods. The sorting by currents was minimal.

MIS 3, 2, and 1 are surprisingly alike in the cores. They both consist of clusters with no prominent indication of current influence. It can evidence that the currents were slower than before during this period, and other factors will support this implication later. Apparently, the current during glacial MIS 2 was not as slow as during MIS 4. The small-scale changes

in strength of the flow were not pronounced in the record probably due to a lower sampling resolution in the upper parts of the cores. Core 13 does not show many similarities with other cores regarding MIS 1, implying that this layer can be even thinner and not seen at this sampling resolution.

The conclusion can be made that cluster analysis gives good results on the identification of features of each period when working with high-resolution cores. The results support the hypothesis of lack of deposition in Core 13 from the second half of MIS 5 to MIS 2. The precise timing of the beginning of MIS 1 has not been determined though.

5.7. Reconstruction of the environment and activity of currents

5.7.1. Dynamics of the position of the current and its influence on sedimentation

The change in position of the current in a channel's profile and its influence on the sedimentation mode can be investigated by imaging sediments layers and a current's strength, using the combination of echo-sounding data, preliminary age model and $\overline{SS}$ record (Fig. 24). Based on a shape of profile (symmetry and sedimentation rate) and supposed strength of a current, the position of the strongest current's vector was determined. Firstly, the choice of the direction of the flow should be explained. There are two quite solid arguments for the flow direction from north-west to south-east. One is the shape of the channel looking from above (Fig. 23): it is narrow on the north-west and wide on the south-east what corresponds to the expected morphology when the energy dissipates during the movement causing sediments deposition downstream, what happens with submarine canyons and channels (Puig et al., 2014). The evidence for the second argument is seen in the profile: earlier the profile was relatively symmetric, later the sedimentation on the south-western part slowed down and even reached zero while north-eastern slope gained a much greater amount of sediments. This indicates movement of a center of the current in northeastern direction. It has been proven that submarine channels are subject to Coriolis force (Cossu et al., 2015) meaning movement of the vector of a flow to the right from the direction in Northern hemisphere and to the left in Southern hemisphere. Applying this principle to the case of our study gives the result of southeastern directed flow (Fig. 23). This proves an assumption of Woodgate et al., 2001 about an intermediate depth current that detaches from a northward flowing current to the west of the Ridge, turns to the south-east and moves to the Makarov Basin.

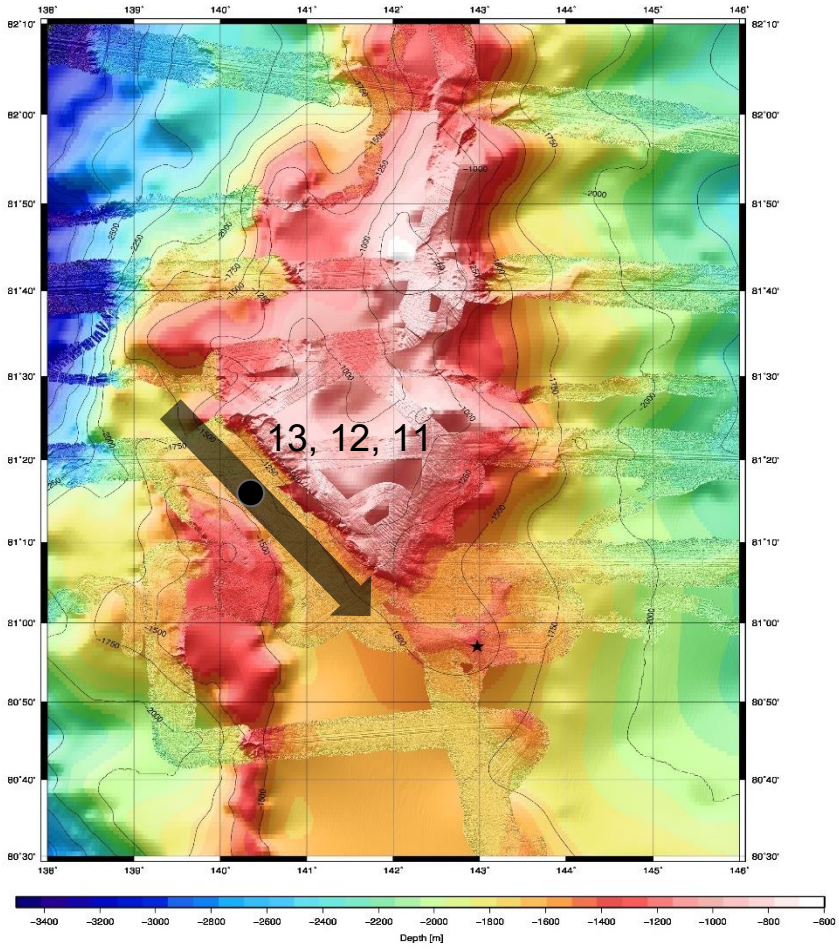

Figure 23. Bathymetry chart of the area (Stein, 2019). Black dot indicates position of the cores, gray arrow – supposed direction of the current.

Changes in the current's position can explain paradoxical sedimentation rates. The currents were the strongest at the beginning of the period (MIS 7-6), yet the sedimentation rates were very high. Later the current became weaker accompanying surprisingly low rates of deposition. The reconstructed picture (Fig. 24) demonstrates that earlier the profile was quite flat and the channel was wide, supposedly evidencing that the current was constantly changing its position so that the energy was equally distributed on the bottom, leading to high uniform sedimentation. After MIS 6 the current concentrated in the south-western part, probably meeting a rocky slope to the right of its direction, thus narrowing channel down. The grain-size data supports this as the evidence of winnowing (coarsening) was observed on the bottom of the channel while the flank experienced accumulation of finer particles, supposedly redeposited from the center of the channel. Later, even though the current's speed was not great, the deposition could not be fast due to high energy concentration. Apparently, during MIS 1 the current started to meander again (probably because it became shallower), leading to a thin sediment cover all over the channel. Such behavior is a common feature of the submarine channels (Sylvester et al., 2011). Apparently, a downcore grain-

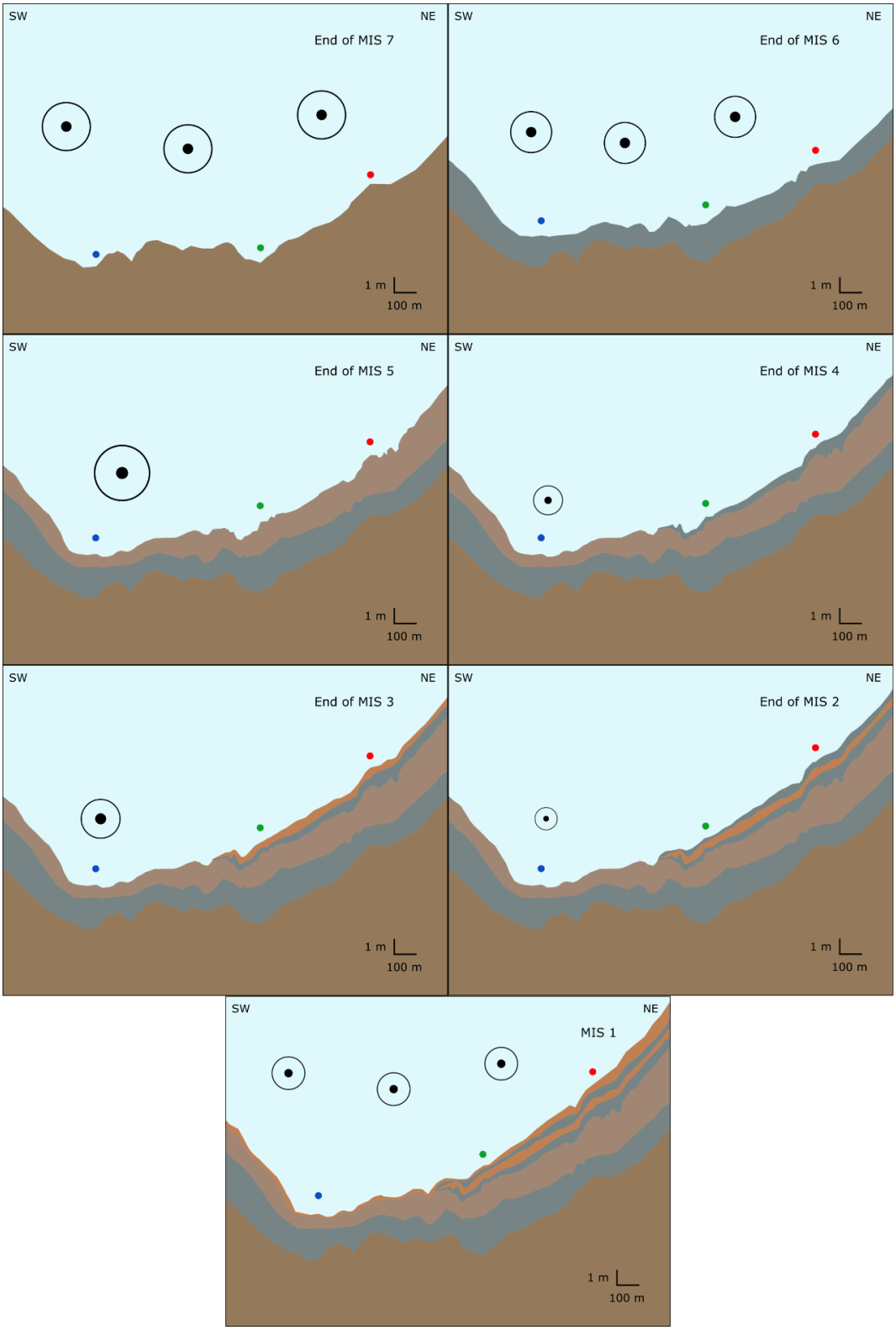

Figure 24. Evolution of the morphology and sedimentation of channel, position and strength of the current during the end of MIS 7 – present time. The dots indicate position of the cores: red – 11, green – 12, blue – 13. Circles with dots show the currents' direction and strength.

size fluctuations can reveal not only a temporal change in strength of a current but the position of a current in a profile (Revel et al., 1996).

Based on that, the dynamics of the position of the current can be summarized. There is evidence that it has gradually slowed down in the studied area, and it happened more actively on the slope than in the middle of the channel. Apart from that, it has been moving in the south-western direction. An implication can be made that the flow will elevate again and spear over the channel, causing uniform deposition.

5.7.2 Changes of the sedimentological environment during the covered period

The results of numerous analyses allow reconstructing the environment and conditions of sedimentation in the channel during the covered period i.e., from the second half of MIS 7 to the present day. In order to create a generalized simplified picture for the area, average of the parameters in cores 11 and 12 was plotted for every MIS along with the data on core 13. The parameters demonstrating major differences between MIS are represented in Fig. 25 A-C.

TOC does not show any periodic variations; the content is quite low during the whole period, as expected in the Arctic Ocean with relatively low production (Stein and Macdonald, 2004). Two prominent peaks are seen: during MIS 6, excluding core 13, and MIS 1. The first one reflects expected TOC content during the cold period, as the environmental conditions were favorable for organic matter preservation (Stein, 2008). The bottom of the channel could have been already under the influence of the intense current at that time, leading to reduced biota conservation. The peak on the surface is probably caused by high biomass of living organisms which have not been reworked.

$\overline{SS}$ record reflects consecutive alternations of high and low numbers during every MIS. Stronger current in an interglacial period was always followed by a deceleration during glacial. It coincides with the results of several paleocurrent studies which supposed a connection between current speed and glaciations: there was evidence that the currents are stronger during interglacials (Bianchi and McCave, 1999; Knutz, 2008; McCave and Andrews, 2019).

Moreover, the general decreasing in time trend is seen. Nevertheless, in Core 13 the current was apparently the strongest during MIS 4-2, as the flow of water with particles went by without any deposition or even eroding the bottom.

Sand record recalls that of $\overline{SS}$, although a gradual decrease is observed during MIS 4-2, while there is a peak of $\overline{SS}$ in MIS 3. Similar character of distribution in earlier periods can indicate current-sorted nature of this fraction, especially considering that at that time water flow was the strongest. A difference between sand distribution and $\overline{SS}$ later evidences about diverse nature of their deposition, thus supporting IRD presence in MIS 4 as it was supposed earlier. Moreover, change in a current's mode explains a lower amount of coarse fraction on the flank of a channel: as the flow concentrated in the south-east after MIS 6, the winnowing became weaker on the northeastern flank while the deposition of the fine fractions, lifted by the flow from the bottom of the channel, enhanced.

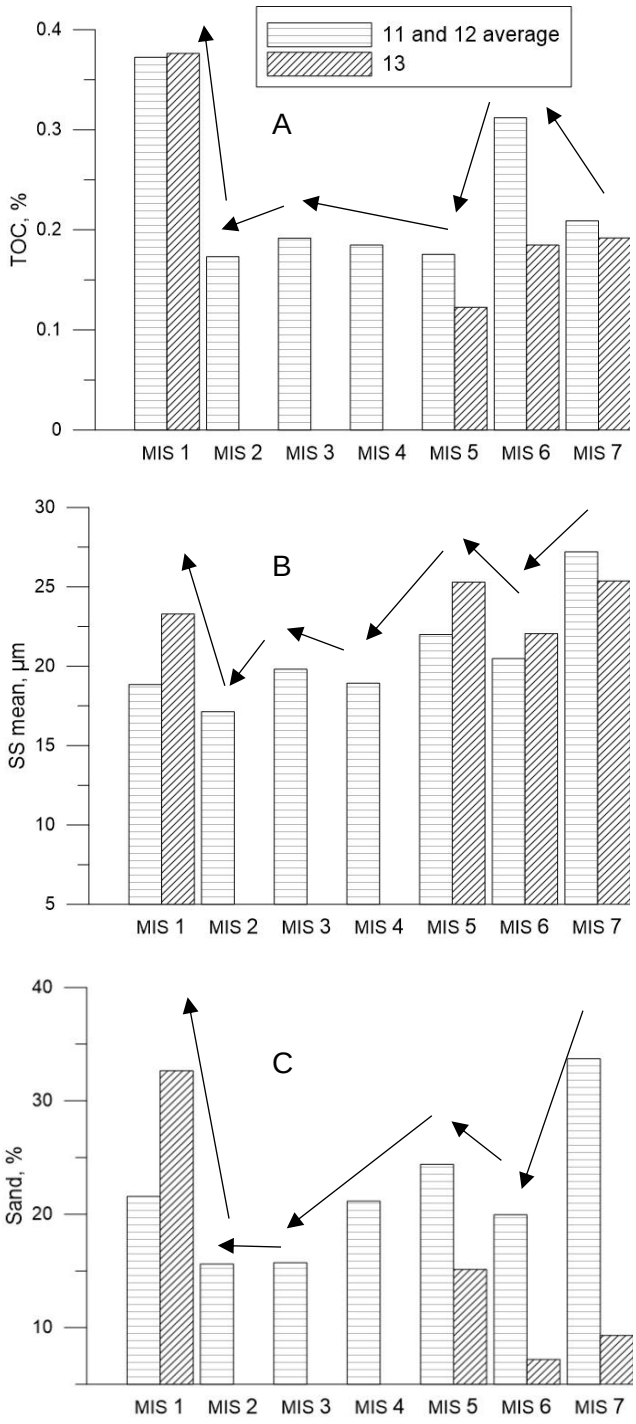

Figure 25. Bar-charts of TOC (A), $\overline{SS}$ (B) and sand content (C) averaged for cores 11 and 12 and in Core 13. Arrows indicate major changes between MIS.

5.7.3. Water composition and climate as main factors of circulation

As it was emphasized in Chapter 2, the Arctic Ocean is a semi-enclosed basin strongly depending on external input of water, particularly from the northern Atlantic Ocean. Apart from that, the formation of sea ice along the continental margins leads to a brine water formation (Shapiro et al., 2003). Such composition makes it possible to distinguish these two types of water and change of the balance between them in the past. The study of Haley et al., 2008 uses the ratio of neodymium isotopes from the metal-oxide coatings of the sediment in order to reconstruct the composition of Arctic Intermediate Water. The reconstruction showed considerably high Atlantic Water input during warm periods, and domination of brines input during glacials MIS 6 and 4 (Fig. 26). This variability coincides with our $\overline{SS}$ records indicating stronger flows during warm periods, making the connection between Atlantic Water input and the speed of currents clear. Even the relatively high $\overline{SS}$ during MIS 2 coincides with unexpectedly low brine formation. The increased role of the Atlantic water during this period is explained by the lack of ice sheet on the Kara Sea shelf region after 50 kyr (Svendsen et al., 2004), what led to the reduced brine input.

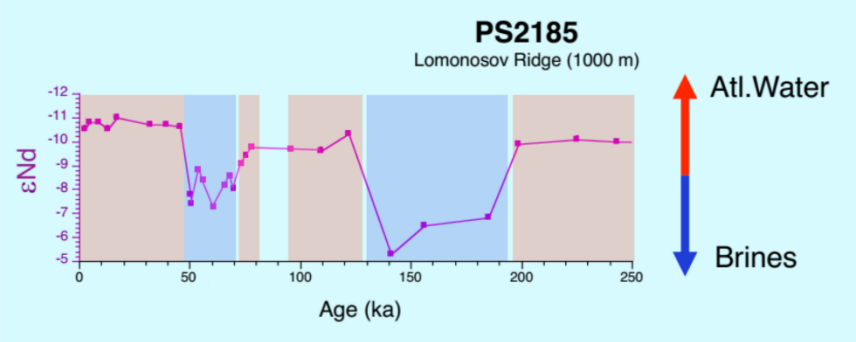

Figure 26. Nd isotopes ratio during last 250 ka; blue areas indicate periods of low Atlantic water input and coincide with MIS 6 and MIS 4 (Haley et al., 2008, modified by R. Spielhagen, 2017).

Climate changes are the reason for the periodicity of water composition: low temperatures cause extensive glaciations which create a thick layer of cold brine water on the surface, thus, deepening halocline and inhibiting stratification, causing the saline Atlantic water flows to sink and preventing their penetration far to the East (McCave and Hall, 2006). Moreover, the formation of Atlantic Intermediate Water happened further south in the North Atlantic (Ganopolski et al., 1998), limiting the influence on the Arctic Ocean. During warmer times the cold halocline was thinner and closer to the surface, the stratification was enhanced and the intermediate water from Atlantic formed close to the north and reached further east (Haley et al., 2008; Hoffman, 2019; Jakobsson et al., 2014; Knutz, 2008; Stein, 2008).

It has been known that the Lomonosov Ridge is the largest obstacle for the water flowing from the Atlantic to the east, dividing the ocean into two large basins and creating a difference in water composition. Some part of the water reaches Amerasian Basin as contour currents along the Eurasian shelf bypassing the ridge. Yet, there was evidence that intermediate layers go through the ridge (see Chapter 1). This study reveals that the channel with water depth only about 1700 m can be used for such purpose.

6. Conclusions and outlook

The paleo-current activity was reconstructed in a channel in the Southern Lomonosov Ridge near the Eurasian shelf at 1700 m water depth covering the time period from the end of MIS 7 to present days. Grain-size and total organic carbon data from three gravity-cores were used. Quite low TOC contents, characteristic for this area, were revealed. Dominating sediments were very fine in grain-size: clayey silt and silty clay, yet numerous layers with strong sand presence were discovered.

Sortable silt mean size was the main proxy applied for the reconstruction of the currents' speed. A strong influence of currents on the sedimentation was indicated in some parts of all three studied cores. The attempt to distinguish between IRD and coarse particles transported by currents was made; weak positive correlation of the sand fraction with the sortable silt mean supposed that the currents were strong enough to transport sand; therefore, this fraction consisted from IRD only partially. Yet, several peaks of IRD input were detected during the terminations.

The sedimentation pattern demonstrated features of a contourite system: lower rates of deposition at the bottom of a moat and accumulation at the flank. The combination of the age model, sedimentation rates and grain-size data allowed to reconstruct the dynamics of the intermediate water flow. Both temporal and spatial changes in current speed, as well as the direction of the current, were revealed. Based on this reconstruction, the current flowing from north-west to south-east during the whole period has experienced a gradual decrease in strength. It was assumed that the flow was widely distributed over the channel during MIS 7-6 leading to a high sedimentation rate all over the cores sites, then it became reduced and concentrated along the south-western slope where the increase in energy caused extremely low deposition and erosion together with a coarsening. The north-eastern flank was subject to an active deposition of fine-grained sediments, transported by the current.

Periods of stronger flow generally coincided with the interglacial stages and terminations. It was explained by an active Atlantic Water inflow into the Arctic Ocean during interglacial

stages, when several factors influenced the formation of water masses, such as the formation of water closer to the north and stronger stratification allowing for the intermediate water to reach further east. This evidences that water from the Atlantic Ocean could not only go into the Makarov Basin as a contour current along the shelf slope but also cross the Lomonosov Ridge through the channel.

Therefore, this study can be considered as a successful application of the sortable silt mean approach as a current speed proxy in the Arctic Ocean. Nevertheless, some aspects can be improved and developed. In order to precisely distinguish IRD in the sediments, a more detailed study of the coarse fraction should be performed, such as mineralogical and grain shape analyses. For a more precise determination of the timing of water inflows and current-controlled processes, the existing age model has to be improved significantly. In this context, the period of special interest is the last interglacial MIS 5 with its sub-stages which did not receive close inspection in the current study. Furthermore, for reconstructing the long-term history and evolution of the channel during Cenozoic times, seismic data could be used.

Acknowledgements

I would like to thank Saint Petersburg State University, Hamburg University and University of Bremen, Federal Ministry of Education and Research, project The Changing Arctic Transpolar System (CATS), 03F0776, and Polar and Marine Sciences master program POMOR for the opportunity to write this master thesis using the knowledge acquired both in Russia and Germany.

I thank my supervisor from German side Prof. Dr. Rüdiger Stein (AWI) for an invitation to the expedition Polarstern 115/2 as well as useful comments and advise on the work, and, of course, the idea. I thank my supervisor from Russian side Dr. Alexey Krylov (SPSU) for the valuable remarks and questions.

I also thank captain and crew of *RV Polarstern* together with scientific group onboard, especially the geology party, for the assistance with the fieldwork.

Moreover, I am grateful to:

- AWI for providing me with access to the laboratories and help of the technicians (Valéa Schumacher and others);
- Dr. Frank Niessen (AWI) for the echo-sounding and physical properties data;
- Sergei Freiman (Moscow State University) for the fruitful discussion on the topic.

References

Aagaard, K., Swift, J. H., and Carmack, E. C., 1985. Thermohaline circulation in the Arctic Mediterranean Seas. Journal of geophysical research, 90: 4833–4846.

Andrews, J.T., 2011. Unravelling sediment transport along glaciated margins (the northwestern Nordic Seas) using quantitative X-ray diffraction of bulk (< 2 mm) sediment. In: Bhuiyan, A.F. (Ed.), Sediment Transport. InTech, 225–248.

Andrews, J.T., Klein, A.J., Jenner, K.A., Jennings, A.E., and Campbell, C., 2018. The variability of Baffin Bay seafloor sediment mineralogy: the identification of discrete glacial sediment sources and application to Late Quaternary downcore analysis. Can. J. Earth Sci., 55: 620–639.

Bianchi, G. G. and McCave, I. N., 1999. Holocene periodicity in North Atlantic climate and deep-ocean flow south of Iceland. Nature, 397: 515–517.

Bischof, J., Clark, D.L., and Vincent, J.-S., 1996. Origin of ice-rafted debris: Pleistocene paleoceanography in the Western Arctic Ocean. Paleoceanography, 11 (6): 743–756.

Bluhm, B. A., Kosobokova, K. N., and Carmack, E. C., 2015. A tale of two basins: An integrated physical and biological perspective of the deep Arctic Ocean. Progress in Oceanography, 139: 89–121.

Chaddock, R. E., 1925. Principles and Methods of Statistics. Boston, Houghton Mifflin Company, 471 p.

Clark, D.L., Whitman, R.R., Morgan, K.A., and Mackay, S.D., 1980. Stratigraphy and glacial-marine sediments of the Amerasian Basin, central Arctic Ocean. Spec. Pap. — Geol. Soc. Am. 181: 1–57.

Cochran, J. R., Edwards, M. H., and Coakley, B. J., 2006. Morphology and structure of the Lomonosov Ridge, Arctic Ocean. Geochem. Geophys. Geosyst., 7: 26 p.

Coope, G.R., Lemdahl, G., Lowe, J.J. and Walkling, A.,1999. Temperature gradients in northern Europe during the last glacial – Holocene transition (14–9 ^{14}C kyr BP) interpreted from coleopteran assemblages. Journal of Quaternary Science, 13(5): 419–433.

Cossu, R., Wells, M. G., and Peakall, J., 2015. Latitudinal variations in submarine channel sedimentation patterns: the role of Coriolis forces. Journal of the Geological Society, 172(2): 161–174.

Darby, D.A., Bischof, J.F., and Jones, G.A., 1997. Radiocarbon chronology of depositional regimes in the western Arctic Ocean. Deep-Sea Research II 44 (8): 1745–1757.

ELTRA Elemental Analyzers, 2013. Carbon / Sulfur Analyzers CS-800 | CS-2000, brochure 99000-0001/E-05-2013, Eltra GmbH, Germany

Faugères, J. C. and Mulder, T., 2011. Contour currents and contourite drifts. Developments in Sedimentology, 63(C): 149–214.

Folk, R.L. and Ward, W.C., 1957. Brazos River bar: a study in the significance of grain size parameters. Journal of Sedimentary Petrology, 27: 3–26.

Ganopolski, A., Rahmstorf, S., Petoukhov, V., and Claussen, M., 1998. Simulation of modern and glacial climates with a coupled global model of intermediate complexity. Nature, 391: 351–356.

Haley, B. A., Frank, M., Spielhagen, R. F., and Eisenhauer, A., 2008. Influence of brine formation on Arctic Ocean circulation over the past 15 million years. Nature Geoscience, 1(1): 68–72.

Hass, H. C., 2002. A method to reduce the influence of ice-rafted debris on a grain size record from northern Fram Strait, Arctic Ocean. Polar Research 21(2): 299–306.

Henrich, R., Kassens, H., Vogelsang, E., and Thiede, J., 1989. Sedimentary facies of glacial-interglacial cycles in the Norwegian Sea during the last 350 ka. Marine Geology, 86: 283–319.

Hjulstrom, F., 1935. Studies of Morphological Activity of Rivers as illustrated by the River Fyris. Bulletin of the Geological Institute University of Uppsala, 25: 221–527.

Hoffmann, S. S., Dalsing, R. E., and Murphy, S. C., 2019. Sortable silt records of intermediate-depth circulation and sedimentation in the Southwest Labrador Sea since the Last Glacial Maximum. Quaternary Science Reviews, 206: 99–110.

Ikeda, M., Tanaka, S. S., and Watanabe, Y. W., 2018. Circulation patterns in the lower Arctic Ocean derived from geochemical data. Journal of Oceanography, 74(5): 453–470.

Jakobsson, M., 2002. Hypsometry and volume of the Arctic Ocean and its constituent seas. Geochem. Geophys. Geosyst., 3: 1–18.

Jakobsson, M., Grantz, A., Kristoffersen, Y., and Macnab, R., 2003. Physiographic provinces of the Arctic Ocean seafloor. GSA Bull., 115 (11): 1443–1455.

Jakobsson, M., Andreassen, K., Bjarnadóttir, L. R., Dove, D., Dowdeswell, J. A., England, J. H., Funder, S., Kelly Hogan, K., Ingólfsson, Ó., Jennings, A. E., Larsen, N. K., Kirchner, N., Landvik, J. Y., Mayer, L. A., Mikkelsen, N., Möller, P., Niessen, F., Nilsson, J., O'Regan, M., Polyak, L., Nørgaard-Pedersen, N., and Stein, R., 2014. Arctic Ocean glacial history. Quaternary Science Reviews, 92: 40–67.

Jakobsson, M., Backman, J., Rudels, B., Nycander, J., Frank, M., Mayer, and L., Moran, K., 2007. The early Miocene onset of a ventilated circulation regime in the Arctic Ocean. Nature, 447: 986–989.

Jennings, A. E., Hald, M., Smith, M., and Andrews, J. T., 2006. Freshwater forcing from the Greenland Ice Sheet during the Younger Dryas: evidence from southeastern Greenland shelf cores. Quaternary Science Reviews, 25: 282–298.

Jones, E. P., 2001. Circulation in the Arctic Ocean. Polar Research 20(2): 139–146.

Jonkers, L., Barker, S., Hall, I. R., and Prins, M. A., 2015. Correcting for the influence of ice-rafted detritus on grain size-based paleocurrent speed estimates. Paleoceanography, 30: 1347–1357.

Knutz, P. C., 2008. Chapter 24. Palaeoceanographic Significance of Contourite Drifts. In: Rebesco, M., Camerlenghi, A. (eds.), Developments in Sedimentology, Contourites, 60(08). Elsevier, 511–535.

Lamy, F., Arz, H. W., Kilian, R., Lange, C. B., Lembke-Jene, L., Wengler, M., Kaiser, J., Wenglera, M., Kaiserb, J., Baeza-Urreac, O., Hallf, I. R., Haradag, N., and Tiedemann, R., 2015. Glacial reduction and millennial-scale variations in Drake Passage throughflow. PNAS, 112(44): 13496–13501.

Lantzsch, H., Hanebuth, T. J. J., Horry, J., Grave, M., Rebesco, M., and Schwenk, T., 2017. Deglacial to Holocene history of ice-sheet retreat and bottom current strength on the western Barents Sea shelf. Quaternary Science Reviews, 173: 40–57.

Laukert, G., Frank, M., Bauch, D., Hathorne, E. C., Rabe, B., Appen, W. Von, and Zieringer, M., 2017. Ocean circulation and freshwater pathways in the Arctic Mediterranean based on a combined Nd isotope, REE and oxygen isotope section across Fram Strait. Geochimica et Cosmochimica Acta, 202: 285–309.

Ledbetter, M. T., 1986. A late Pleistocene time-series of bottom-current speed in the Vema Channel. Palaeogeogr. Palaeoclimatol. Palaeoecol., 53: 97–105.

Lewis, A.R., Marchant, D.R., Ashworth, A.C., Hemming, S.R., and Machlus, M.L., 2007. Major middle Miocene global climate change: Evidence from East Antarctica and the Transantarctic Mountains. GSA Bulletin, 119 (11-12): 1449–1461.

Lisiecki, L.E. and Raymo, M.E., 2005. A Pliocene-Pleistocene stack of 57 globally distributed benthic $d^{18}O$ records. Paleoceanography, 20: 17 p.

Li, N., Yang, X., Peng, J., Zhou, Q., and Su, Z., 2019. Deep-water bottom current evolution in the northern South China Sea during the last 150kyr: Evidence from sortable-silt grain size and sedimentary magnetic fabric. Journal of Asian Earth Sciences, 171: 78–87.

Lototskaya A. and Ganssen G. M., 1999. The structure of Termination II (penultimate deglaciation and Eemian) in the North Atlantic. Quaternary Science Reviews, 18 (14): 1641–1654.

Mora, C.I., Driese, S.G., and Colarusso, L. A., 1996. Middle to Late Paleozoic Atmospheric CO_2 Levels from Soil Carbonate and Organic Matter. Science, 271 (5252): 1105.

Revel M., Cremer M., and Grousset F.E., 1996. Grain-size and Sr-Nd isotopes as tracer of paleo-bottom current strength, Northeast Atlantic Ocean. Marine Geology, 13: 233–249.

Mao, L., Piper, D. J. W., Saint-Ange, F., and Andrews, J. T., 2018. Labrador Current fluctuation during the last glacial cycle. Marine Geology, 395: 234–246.

Mauritzen C., Rudels B., and Toole J., 2013. The Arctic and Subarctic oceans/seas. In: Siedler G., Griffies S.M., Gould J, and Church J.A. (eds.), Ocean circulation and climate. Amsterdam: Academic Press, 443–470.

McCave, I. N., Manighetti, B., and Robinson, S. G., 1995. Sortable Silt and Fine Sediment Size/Composition Slicing: Parameters for Palaeocurrent Speed and Palaeoceanography. Paleoceanography, 10(3): 593–610.

McCave, I. N., 2008. Chapter 8. Size Sorting During Transport and Deposition of Fine Sediments: Sortable Silt and Flow Speed. In: Rebesco, M., Camerlenghi, A. (eds.), Developments in Sedimentology, Contourites, 60(08). Elsevier, 121–142.

McCave, I. N., Thornalley, D. J. R., and Hall, I. R., 2017. Relation of sortable silt grain-size to deep-sea current speeds: Calibration of the 'Mud Current Meter'. Deep-Sea Research Part I: Oceanographic Research Papers, 127: 1–12.

McCave, I. N. and Andrews, J. T., 2019. Distinguishing current effects in sediments delivered to the ocean by ice. I. Principles, methods and examples. Quaternary Science Reviews, 212: 92–107.

McCave, I. N. and Hall, I. R., 2006. Size sorting in marine muds: Processes, pitfalls, and prospects for paleoflow-speed proxies. Geochem. Geophys. Geosyst., 7: 37 p.

Moseley, G. E., Spötl, C., Cheng, H., Boch, R., Min, A., and Edwards, R. L., 2015. Termination-II interstadial/stadial climate change recorded in two stalagmites from the north European Alps. Quaternary Science Reviews, 127: 229–239.

Obrochta, S. P., Crowley, T. J., Channell, J. E. T., Hodell, D. A., Baker, P. A., Seki, A., and Yokoyama, Y., 2014. Climate variability and ice-sheet dynamics during the last three glaciations. Earth and Planetary Science Letters, 406: 198–212.

Oppo, D. W., Keigwin, L. D., and McManus, J. F., 2001. Persistent suborbital climate variability in marine isotope. Paleoceanography, 16(3): 280–292.

Piskarev, A. L., Butsenko, V. V, Chernykh, A. A., Ivanov, M. V, Kaminsky, V. D., Poselov, V. A., and Savin, V. A., 2018. Lomonosov Ridge. In: Piskarev A., Poselov V., Kaminsky V. (eds), Geologic Structures of the Arctic Basin. Springer, Cham, 157–185.

Proshutinsky, A., Dukhovskoy, D., Timmermans, M., Krishfield, R., and Bamber, J. L., 2015. Arctic circulation regimes. Phil. Trans. R. Soc. A, 373: 18 p.

Puig, P., Palanques, A., and Martín, J., 2014. Contemporary Sediment-Transport Processes in Submarine Canyons. Annual Review of Marine Science, 6(1): 53–77.

Rebesco, M., Hernández-Molina, F. J., Van Rooij, D., and Wåhlin, A., 2014. Contourites and associated sediments controlled by deep-water circulation processes: State-of-the-art and future considerations. Marine Geology, 352: 111–154.

Rudels, B., Jones, E. P., Anderson, L. G., and Kattner, G., 1994. On the Intermediate Depth Waters of the Arctic Ocean. In: Johannessen, O. M., Muench, R. D., and Overland, J. E. (eds.), The Polar Oceans and Their Role in Shaping the Global Environment. Geophysical monograph, 85. American Geophysical Union, 33–46.

Rudels, B., 2015. Arctic Ocean circulation, processes and water masses: A description of observations and ideas with focus on the period prior to the International Polar Year 2007 – 2009. Progress in Oceanography, 132: 22–67.

Rudels, B., Korhonen, M., Schauer, U., Pisarev, S., Rabe, B., and Wisotzki, A., 2015. Circulation and transformation of Atlantic water in the Eurasian Basin and the contribution of the Fram Strait inflow branch to the Arctic Ocean heat budget. Progress in Oceanography, 132: 128–152.

Rudels, B., 2018. Arctic Ocean Circulation. In: Cochran, J. K., Bokuniewicz, H. J., Yager, P.L. (eds.), Encyclopedia of Ocean Sciences (3rd ed.). Elsevier Inc. Academic Press, 262–277.

http://www.r-project.org The R Project for Statistical Computing, accessed on February 20 2019

SediGraph III PLUS Particle Size Analyzer brochure 512/42705/00 Micromeritics Instrument Corporation, USA

Shapiro, G. I., Huthnance, J. M., and Ivanov, V. V., 2003. Dense water cascading off the continental shelf. J. Geophys. Res., 108: 3390.

Smillie, Z., Stow, D., and Esentia, I., 2018. Deep-Sea Contourites Drifts, Erosional Features and Bedforms. In: Cochran, J. K., Bokuniewicz, H. J., Yager, P.L. (eds.), Encyclopedia of Ocean Sciences, (3rd ed.). Elsevier Inc. Academic Press, 97–110.

Spall, M. A., 2013. On the Circulation of Atlantic Water in the Arctic Ocean. J. Phys. Oceanogr., 43: 2352–2371.

Spielhagen, R. F., Baumann, K. H., Erlenkeuser, H., Nowaczyk, N. R., Nørgaard-Pedersen, N., Vogt, C., and Weiel, D., 2004. Arctic Ocean deep-sea record of northern Eurasian ice sheet history. Quaternary Science Reviews, 23(11–13): 1455–1483.

Stein, R., 1985. Rapid grain-size analyses of clay and silt fraction by SediGraph 5000D: Comparison with Coulter Counter and Atterberg methods. Journal Of Sedimentary Research, 55(4): 590–593.

Stein, R., 2008. Arctic Ocean Sediments: Processes, Proxies, and Paleoenvironment. Oxford, Elsevier, 602 p.

Stein, R. (Ed.), 2015. The Expedition PS87 of the Research Vessel POLARSTERN to the Arctic Ocean in 2014. Reports on Polar and Marine Research, Bremerhaven, Alfred Wegener Institute for Polar and Marine Research, 688: 273 p.

Stein, R., Fahl, K., Gierz, P., Niessen, F., and Lohmann, G., 2017. Arctic Ocean sea ice cover during the penultimate glacial and the last interglacial. Nature Communications, 8: 373.

Stein, R. (Ed.), 2019. The Expedition PS115/2 of the Research Vessel POLARSTERN to the Arctic Ocean in 2018. Reports on Polar and Marine Research, Bremerhaven, Alfred Wegener Institute for Polar and Marine Research, 728: 249 p.

Stein, R. and Macdonald, R. W., 2004. Geochemical Proxies used for Organic Carbon Source Identification in Arctic Ocean Sediments. In: Stein, R. and Macdonald, R. W. (Ed.), The organic carbon cycle in the Arctic Ocean. Springer, 24–32.

Stow, D. A. V., Hunter, S., Wilkinson, D., and Hernández-Molina, F. J., 2008. Chapter 9. The Nature of Contourite Deposition. In: Rebesco, M., Camerlenghi, A. (eds.), Developments in Sedimentology Contourites, 60(08). Elsevier, 143–156.

Stroeve, J. and Notz, D., 2018. Changing state of Arctic sea ice across all seasons. Environ. Res. Lett., 13: 24 p.

Svendsen, J.I., Alexanderson, H., Astakhov, V.I., Demidov, I., Dowdeswell, J.A., Funder, S., Gataullin, V., Henriksen, M., Hjort, C., Houmark-Nielsen, M., Hubberten, H.W., Ingølfsson, Ó., Jakobsson, M., Kjær, K.H., Larsen, E., Lokrantz, H., Lunkka, J.P., Lysså, A., Mangerud, J., Matiouchkov, A., Murray, A., Möller, P., Niessen, F., Nikolskaya, O., Polyak, L., Saarnisto, M., Siegert, C., Siegert, M.J., Spielhagen, R.F., and Stein, R., 2004. Late quaternary ice sheet history of northern Eurasia. Quaternary Science Reviews, 23 (11–13): 1229–1271.

Swift J.H. and Koltermann K.P., 1988. The origin of Norwegian Sea deep water. J. Geophys. Res.: Oceans, 93 (C4): 3563–3569.

Sylvester, Z., Pirmez, C., and Cantelli, A., 2011. A model of submarine channel-levee evolution based on channel trajectories: Implications for stratigraphic architecture. Marine and Petroleum Geology, 28(3): 716–727.

Thomas, A. L., Henderson, G. M., and McCave, I. N., 2006. Constant flow of AABW into the Indian Ocean over the past 140 ka? Conflict between $^{231}Pa/^{230}Th$ and sortable silt records. Goldschmidt Conference Abstracts: 647.

Wang, R., Polyak, L., Xiao, W., Wu, L., Zhang, T., and Sun, Y., 2018. Late-Middle Quaternary lithostratigraphy and sedimentation patterns on the Alpha Ridge, central Arctic Ocean: Implications for Arctic climate variability on orbital time scales. Quaternary Science Reviews, 181: 93–108.

Woodgate, R., 2012. Arctic Ocean Circulation: Going Around At the Top Of the World. Nature Education Knowledge, 4(8): 1–13.

Woodgate, R. A., Aagaard, K., Muench, R. D., Gunn, J., Rudels, B., Roach, A. T., and Schauer, U., 2001. The Arctic Ocean Boundary Current along the Eurasian slope and the adjacent Lomonosov Ridge: Water mass properties, transports and transformations from moored instruments. Deep-Sea Research, I 48: 1757–1792.

Appendix

The appendix is written on a CD enclosed to the thesis. The content is as follows:

- core photographs (Author: R. Love);

- Excel file with data tables on TOC, grain-size fractions content in % (sand, very coarse silt, coarse silt, medium silt, fine silt, very fine silt, and clay) and calculated parameters ($\overline{SS}$, SS%, $\overline{SS}$ in a phi scale, $\overline{SS}_{pot}$, delta $\overline{SS}$, and sorting/standard deviation) for cores 11, 12, and 13.

Statement on the thesis' originality

Herewith I, Elena Popova, declare that I wrote the thesis independently and did not use any other resources than those named in the bibliography, and, in particular, did not use any internet resources except for those named in the bibliography. The master thesis has not been used previously as part of an examination. The master thesis has not been previously published.

_____ Elena Popova